



Combination Analysis of Multi-Wavelength, Multi-Parameter Radar Measurements for Snowfall

Mariko Oue¹, Pavlos Kollias^{1,2}, Sergey Y. Matrosov³, Alessandro Battaglia^{4,5}, and Alexander V. Ryzhkov⁶

1. Stony Brook University, Stony Brook NY, USA

2. Brookhaven National Laboratory, Upton, NY, USA

3. Cooperative Institute in Research in Environmental Sciences, University of Colorado and NOAA Physical Sciences Laboratory, Boulder, CO, USA

4. Politecnico di Torino, Turin, Italy

5. University of Leicester, Leicester, UK

6. NSSL, University of Oklahoma, Norman, OK, USA

Abstract

Radar dual wavelength ratio (DWR) measurements from the Stony Brook Radar Observatory Ka-band Scanning Polarimetric Radar (KASPR, 35 GHz), a profiling W-band (94 GHz) and a next generation K-band (24-GHz) Micro Rain Radar (MRRPro) were exploited for ice particle identification using triple frequency approaches. The results indicated that two of the radar frequencies (K- and Ka-band) are not sufficiently separated, thus, the triple radar frequency approaches had limited success. On the other hand, a joint analysis of DWR, mean vertical Doppler velocity (MDV), and polarimetric radar variables indicated potential in identifying ice particle types and distinguishing among different ice growth processes and even in revealing additional microphysical details.

We investigated all DWR pairs in conjunction with MDV from the KASPR profiling measurements and differential reflectivity (Z_{DR}) and specific differential phase (K_{DP}) from the KASPR quasi-vertical profiles. The DWR-versus-MDV diagrams coupled with the polarimetric observables exhibited distinct separations of particle populations attributed to different rime degrees and particle growth processes. In fallstreaks, the 35–94 GHz DWR pair increased with the magnitude of MDV corresponding to the scattering calculations for aggregates with lower degrees of riming. The DWR values further increased at lower altitudes while Z_{DR} slightly decreased, indicating further aggregation. Particle populations with higher rime degrees had a similar increase of DWR, but the 1–1.5 m s⁻¹ larger magnitude of MDV and rapid decreases in K_{DP} and Z_{DR} . The analysis also depicted the early stage of riming where Z_{DR} increased with the MDV magnitude collocated with small increases of DWR. This approach will improve quantitative estimations of snow amount and microphysical quantities such as rime mass fraction.

1. Introduction

Millimeter-wavelength (i.e., operating at 35- and 94-GHz) radars have been widely used for the study of liquid and ice precipitation clouds, utilizing their high sensitivity to smaller particles due to Rayleigh scattering and excellent spatiotemporal resolution (Kollias et al., 2007). Cloud radars at 35 GHz and 94 GHz have been routinely operated at surface-based observatories the last two decades (e.g., the European Union CloudNet project and the U.S. Atmospheric Radiation Measurement (ARM) facility, Illingworth et al., 2015; Stokes and Schwartz, 1994; Mather and Voyles, 2013; Kollias et al., 2014; 2016) and from a variety of ship-based (e.g., Lewis et al., 2012) and airborne platforms (e.g., Battaglia et al., 2016; Tridon et al., 2019). Millimeter wavelength



50 radar are particularly suitable for the study of hydrometeors properties (mass, size) using the
presence of non-Rayleigh scattering signals and their higher sensitivity to attenuation. For
example, the dual-wavelength ratio (DWR), the ratio of the longer-wavelength reflectivity to the
shorter-wavelength reflectivity, is affected by the differential scattering and/or attenuation and
depends on the particle size, type, orientation, rime fraction, and radar beam path. DWRs have
been used in multi-wavelength radar measurements for microphysical retrievals such as
55 estimations of liquid water content (e.g., Hogan et al., 2005; Huang et al., 2009; Tridon et al.,
2013; Zhu et al., 2019) and ice water content (IWC, e.g., Matrosov, 1998) and identification of
particle types (e.g., Kneifel et al., 2015; Leinonen and Moisseev, 2015; Moisseev et al., 2015;
Sinclair et al., 2016; Matrosov et al., 2019).

60 Kneifel et al. (2015) illustrated the effectiveness of DWRs to identify ice crystals, aggregates, and
rimed particles, when considering well separated triple radar frequencies (i.e., X, Ka, and W
bands) so that each frequency experiences different scattering regimes. The DWR of X-band to
Ka-band reflectivities (DWR_{XKa}) versus DWR of Ka-band to W-band reflectivities (DWR_{KaW})
diagrams indicated different dependencies on particle type and size. Those curves were in good
agreement with the observed particle types (Kneifel et al., 2016). The triple-frequency capabilities
65 have been used for different frequencies such as S, X, and W bands and Ku, Ka, and W bands
(e.g., Leinonen and Moisseev, 2015; Mason et al., 2019), or even shorter-wavelength radars (e.g.,
Ka, W, and G bands, Lamer et al. 2020). While the triple-frequency approach is a powerful
technique for microphysics research, it requires accurate calibration of the radars, reliable
attenuation correction, careful beam matching, and sufficiently high sensitivities at all frequencies.
70 These conditions are satisfied only in a hand-full of surface observatories.

Another limitation of the triple frequency measurements for ice particle identification is that the
triple frequencies should be well-separated from each other so magnitudes of non-Rayleigh
scattering is different for various DWR pairs and the curves representing a particle type in the
75 DWR correspondence diagram can be distinguished. If the frequencies are too close, then the DWR
trends corresponding to different hydrometeor types may not be sufficiently separated from each
other. For instance, Ka-band (around 35 GHz) frequency and K-band (around 24 GHz) frequency,
which has been employed by a widely-used, low-power, low-cost, high-quality precipitation
profiler, micro rain radar (MRR, e.g., Peters et al., 2002), are rather close, producing similar trends
80 when coupled with a third frequency as shown in Fig. 1. Figure 1a is a DWR_{KKa} versus DWR_{KW}
diagram from the scattering calculations (detailed descriptions of the scattering calculations are
available in Appendix). Similarly, Fig. 1c is a DWR_{XKa} versus DWR_{KaW} diagram. These diagrams
show that the two-DWR space from the three frequency radars exhibits a dependency on ice
particle types, specifically size and rime fraction. However, considering modeling uncertainties
85 and measurement noise, it would be hard to discern the particle types in the K-Ka-W DWR space,
while the X-Ka-W DWR space has larger dynamic ranges likely enough to discern the particle
types as presented in the previous studies. This is, in part, due to the fact that the K-band frequency
(~24 GHz) is not sufficiently separated from the Ka-band frequency (~35 GHz).

It has been shown (e.g., Matrosov et al., 2019) that the DWR also depends on particle shapes (i.e.,
90 aspect ratios defined as the ratio of particle minor and major dimensions). For particles
preferentially oriented with their major dimensions in the horizontal plane, the DWR dependence
on particle shapes is usually strongest for vertically pointing radar measurements and relatively
weak for slant radar viewing (Matrosov, 2021). The impacts of particle shape on the two DWR



pair's diagram (Fig. 1), however, is much smaller than that on individual DWRs for a given
95 frequency pair. To illustrate this point, Figs. 1b and 1d show $DWR_{KKa}-DWR_{KW}$ and $DWR_{XKa}-$
 DWR_{KaW} correspondences, respectively, for a “soft” spheroidal particle model with aspect ratios
0.3 and 0.8. A much weaker particle shape influence on this the $DWR_{KKa}-DWR_{KW}$ field (compared
to individual DWRs) is explained, in part, by the fact that both DWR_{KKa} and DWR_{KW}
increase/decrease as particle become more/less spherical. The similar feature is found in the
100 $DWR_{XKa}-DWR_{KaW}$ field. Particle populations with similar characteristic sizes (color circles in
Figs. 1b and 1d) but different aspect ratios (0.3 vs 0.8), however, produce quite different values of
DWR for both frequency pairs. It is worth also mentioning that a “soft” spheroid particle model
produces $DWR_{KKa}-DWR_{KW}$ correspondences that are similar to those with more sophisticated
models (Fig. 1a vs Fig. 1b).

105 In addition to power measurements, profiling cloud radar can also measure the mean Doppler
velocity (MDV). Although the MDV is affected by the vertical air motion, the community has
developed robust methodologies to use MDV to improve discrimination between the particle types
and ice growth processes (e.g., Orr and Kropfli, 1999; Luke et al., 2010; Protat and Williams,
2011; Kalesse et al., 2013; Schrom and Kumjian, 2016; Oue et al., 2018). Particle fall speed, which
110 is sensitive to rime fraction, is a valuable variable to use to identify particle types (e.g., Locatelli
and Hobbs, 1974; Kajikawa, 1989; Mason et al., 2019). However, using only MDV and reflectivity
measurements would not be enough to distinguish between aggregation and early stage of riming,
because both are associated with very similar fall speeds (e.g., Oue et al., 2016). This study, first
introduces, the use of DWR coupled with MDV to identify particle types that have different degree
115 of riming. Figure 2 shows DWR_{KaW} as a function of MDV and differential MDV ($dMDV = K$ -
band MDV–W-band MDV). The MDV-DWR correspondence is also sensitive to particle size
distribution (PSD) details and rime degree. Fig. 2 indicates only a weak dependency on PSD, which
can be advantageous for distinguishing particle types as PSD influences are minimized.

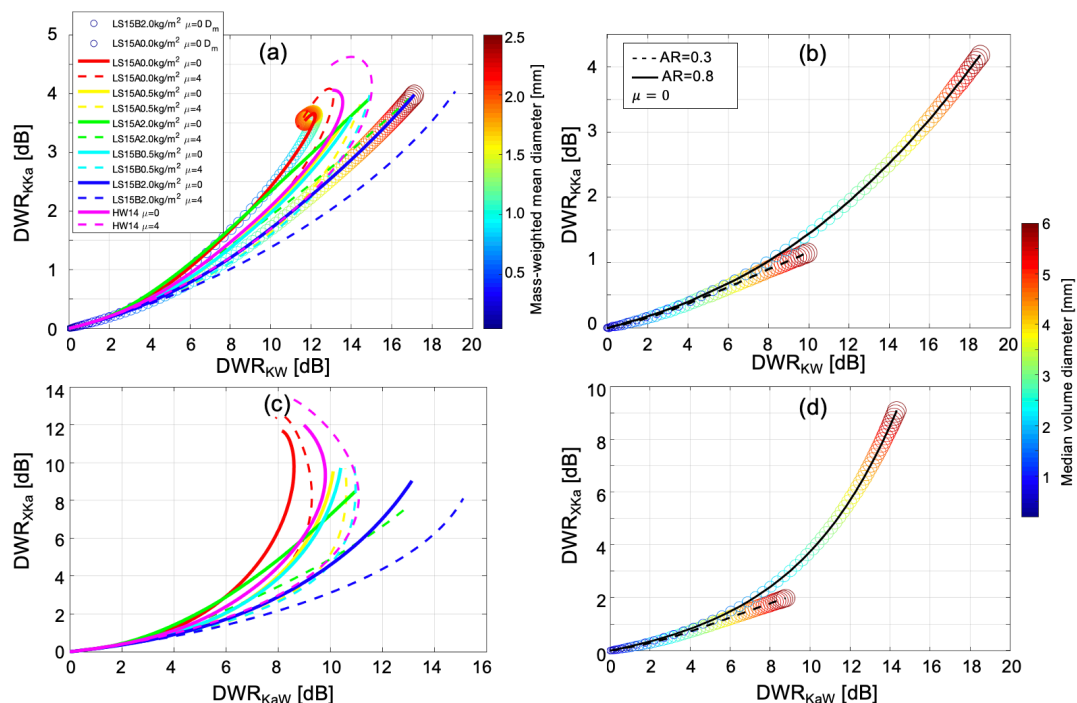
120 Similar to DWR and MDV, polarimetric radar observables are also sensitive to microphysical
properties such as particle type, characteristic size, rime fraction, aspect ratio, canting angle, and
complexity of shape (e.g., Myagkov et al., 2016). These properties provide a constraint on the
particle shapes (i.e., aspect ratio) and help to mitigate the uncertainty in the DWR analysis
mentioned above. The polarimetric variables are particularly suitable to identify depositional,
125 aggregation, and riming growths (e.g., Oue et al., 2016). The most common characteristics of the
polarimetric observables representing the depositional growth are enhancements of differential
reflectivity (Z_{DR}) and specific differential phase (K_{DP}) in a dendritic/plate-like growth regime (e.g.,
around temperature of -15°C), where the ice crystals with small aspect ratios are formed by
depositional growth. The Z_{DR} values decrease with decreasing height in a region of aggregation,
130 while (K_{DP}) often has a maximum just below the Z_{DR} peak. With further height decrease, the aspect
ratios of the individual particles increase (e.g., Vivekanandan et al., 1994; Ryzhkov et al., 1998;
Kennedy and Rutledge, 2011; Andrić et al., 2013; Bechini et al., 2013; Schrom et al., 2015;
Kumjian et al., 2016; Griffin et al., 2018; Matrosov et al., 2020). Similar vertical changes of the
polarimetric variables have been often found in the rime-dominated regions (e.g., Zawadzki et al.,
135 2001; Oue et al., 2016; Giangrande et al., 2016; Kumjian and Lombardo, 2017), as heavy riming
increases particle aspect ratios. Mean particle aspect ratios can be quantitatively estimated using
proxies of radar circular depolarization ratios (e.g., Matrosov et al., 2017). Radar depolarization
ratios can also be used to distinguish among ice hydrometeor types effectively separating oblate
(e.g., plates, dendrites) from prolate (e.g., columns, needles) habits (e.g., Matrosov, 1991;



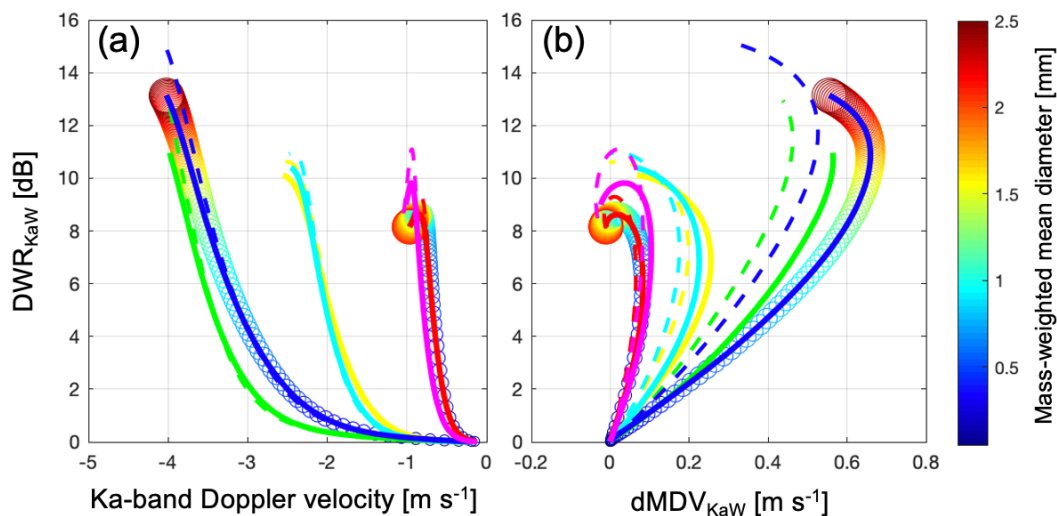
140 Reinking et al., 2002; Matrosov et al., 2012; Oue et al., 2015). Schrom and Kumjian (2016)
suggested that a complementary use of mean vertical Doppler velocity could help to distinguish
the riming process from aggregation-dominated regions. A joint analysis of polarimetric variables
and Doppler spectra by Oue et al. (2018) illustrated a capability of particle type identification in
145 Arctic mixed-phase clouds. However, distinguishing between aggregation and early stage of
riming is still challenging even though MDV and polarimetric variables are jointly used due to the
similar signatures (e.g., Oue et al., 2016).

Winter storms in the Northeast U.S often effect heavy snowfall and destruction of life and property.
The lack of understanding of ice microphysical processes in the storms and poor representation of
150 the ice microphysics parameterizations in numerical cloud models has resulted in large uncertainty
in forecasting snowfall. The ice microphysical processes including depositional, riming, and
aggregation growths often coexist in the snowstorm cloudy volumes (e.g., Kumjian and Lombardo,
2017; Colle et al., 2014), making it difficult to identify the processes in the observations. To
facilitate studies of cloud microphysics and dynamics in the Northeast U.S., the Stony Brook Radar
155 Observatory (SBRO) was established in March in 2017 in Stony Brook University, Stony Brook,
NY (Fig. 3). The flagship radar of the SBRO is a very sensitive, sophisticated, and well-calibrated
Ka-band (35-GHz) scanning fully-polarimetric radar (KASPR). The radar measurements are
complemented by two profiling radar systems operating at W-band (94-GHz, ROGER) and K-
band (24-GHz, MRRPro) and ground-based in-situ sensors. The SBRO radar systems have
160 collected vertically pointing triple frequency reflectivity and Doppler velocity data which were
complemented by polarimetric variables from KASPR for a snowstorm observed on February 20,
2019. The triple frequency measurements showed that the DWR from the dual-wavelength
measurements in conjunction with MDV and polarimetric observations had a higher efficiency to
distinguish ice particle types and growth processes rather than the DWR-only diagrams from triple-
165 frequency measurements. This study first illustrates the capability and advantage of the use of
MDV and polarimetric radar observables in conjunction with DWR measurements to identify
particle types and growth processes in winter storms.

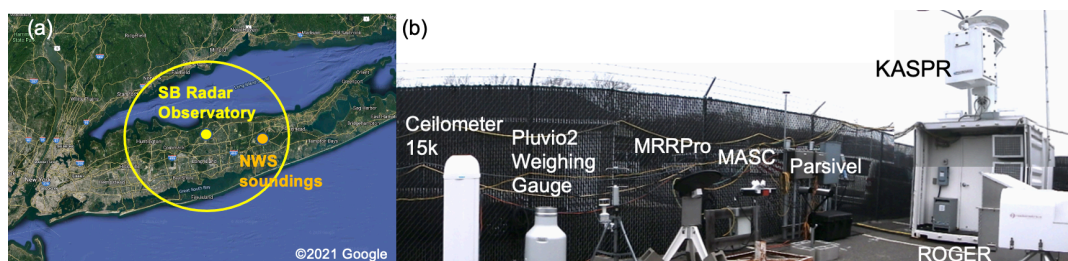
170



175 Figure 1: DWR of K-band (24 GHz) reflectivity to Ka-band (35.5 GHz) reflectivity versus that of
 K-band reflectivity to W-band (94 GHz) reflectivity diagram from (a) the SSRGA scattering
 property database and (b) Matrosov et al. (2019) accounting for particle aspect ratio (AR). (c) and
 180 (d) are the same as (a) and (b), respectively, but for DWR of X-band (10.7 GHz) reflectivity to
 Ka-band reflectivity versus that of Ka-band reflectivity to W-band reflectivity. Line colors in (a)
 and (c) represent particle models listed in Table A1. Solid and dashed lines in (a) and (c) represent
 the PSD's shape parameter (μ) equal to 0 and 4, respectively. Color of circles in (a) represents
 water-equivalent mass-weighted volume diameter (D_m) of each PSD used to calculate DWRs;
 here, D_m values for the particle models of Leinonen and Szyrmer's (2015) unrimed aggregates
 with $\mu = 0$ (solid red line) and aggregates with high rime degree (solid blue line) are presented.
 Solid and dashed lines in (b) and (d) represent AR=0.8 and AR=0.3, respectively. The DWRs in
 185 (b) and (d) were calculated for PSDs with $\mu = 0$ and median volume particle size (color of circles)
 ranging from 0.2 to 6.0 mm.



190 Figure 2: (a) DWR of Ka-band (35.5 GHz) reflectivity to W-band (94 GHz) reflectivity versus Ka-
 band mean Doppler velocity from the SSRGA scattering database with particle fall velocity models
 of Hogan and Westbrook (2017). (b) DWR of Ka-band reflectivity to W-band reflectivity versus
 195 difference between Ka-band MDV and W-band MDV. Negative Doppler velocity in (a) represents
 a downward motion. Color scale and line legends are the same as in Figure 1. These particle models
 can be classified into low (red and magenta), middle (yellow and cyan), and high (blue and green)
 rime degree particles.



200 Figure 3: (a) Location of the Stony Brook Radar Observatory. (b) Instruments deployed at SBRO.
 A big yellow circle in (a) represents the KASPR 30-km observation range.

2. Data

205 SBRO has been in operation since March in 2017 (-73.127E, 40.897N, ~22 km west of a National
 Weather Service sounding site at Upton, NY; <https://you.stonybrook.edu/radar/>). KASPR,
 ROGER, and MRRPro at SBRO collected triple frequency data during a snow event on February
 20, 2019. This is so far the only case where the high-quality, well-calibrated triple frequency
 measurements together with ground-based in-situ measurements for snow particles for the
 evaluation are available. The SBRO site also has ground-based in-situ observation instruments.



210 The in-situ instruments including a Parsivel optical disdrometer and Multi-Angle Snowflake
Camera (MASC, Garrett et al. 2014) were used to evaluate the radar-based particle identifications.
The SBRO operates ceilometers at the SBRO and Brookhaven National Laboratory sites.
Ceilometer backscatter is sensitive to cloud liquid droplets embedded in ice precipitation clouds.
215 A microwave radiometer was also installed at the SBRO site; however, it was not functional during
the precipitation in this study due to significant snow accumulation on the sensor.

2.1. Ka-band Scanning Polarimetric Radar (KASPR)

220 KASPR, a state-of-the-art cloud scanning radar, is capable of collecting Doppler spectra and radar
moments through alternate transmission of horizontally (H) and vertically (V) polarized waves
and simultaneous reception of co-polar and cross-polar components of the backscattered wave with
the beamwidth of 0.32° . Therefore, a full set of polarimetric radar observables is available
including radar reflectivity (Z_{HH}), differential reflectivity (Z_{DR}), differential phase (ϕ_{DP}), co-polar
225 correlation coefficient (ρ_{hv}), linear depolarization ratio (L_{DR}), and cross-polar correlation
coefficient (ρ_{hx}), along with Doppler velocity and spectral width. Specific differential phase (K_{DP})
is estimated using an iterative algorithm proposed by Hubbert and Bringi (1995). The data post-
processing details are described in Oue et al. (2018). The KASPR was calibrated using a corner
reflector technique, providing reliable reflectivity data to calibrate the other two radar data. The
detailed configurations are also available in Kumjian et al. (2020) and Kollias et al. (2020b).

230 During the radar measurements on February 20, 2019, KASPR executed a scanning strategy that
consisted of surveillance (PPI) scans at a 15° elevation angle, a zenith pointing PPI, hemispheric
range-height indicator (HSRHI) scans at four azimuth angles, and a 5-minute vertically pointing
mode (VPT) during which Doppler spectrum data were collected. This pattern was repeated and
235 took approximately 15 minutes to complete. During a 15-min cycle, two 15° -PPI scans were
included, so that we had the 15° -PPI scans every ~ 7 min which were used to produce quasi-vertical
profile products. The PPI and HSRHI scans were performed in a full polarimetry mode with scan
speeds of 6 s^{-1} and 2 s^{-1} , respectively, to collect data with a 30-m range-gate spacing, 0.6° PPI
azimuthal spacing and 0.3° HSRHI elevation spacing. The VPT mode was executed with only
240 horizontally polarized waves transmitted and both horizontally and vertically polarized waves
received. During the VPT mode, the Doppler spectra were collected every second with a 15-m
range-gate spacing and 0.04 m s^{-1} velocity bin spacing. The zenith PPI scans were used to estimate
a systematic bias of Z_{DR} . The Z_{DR} values presented in this study were corrected for the systematic
biases.

245

2.2. 94-GHz (W-band) Frequency Modulated Continuous Wave (FMCW) profiling radar (ROGER)

250 The system was initially developed as an airborne radar and was integrated on the Center for
Interdisciplinary Remotely-Piloted Aircraft Studies Twin Otter aircraft (Mead et al., 2003). In
2017, the system was refurbished with installing 24-inch parabolic dish antennas, and all the
CFMCW electronics, including a new metal frame to hold the antennas, the server computer and
the power supplies, to make it suitable for ground-based observations and easy shipping.

255



260

This radar system is capable of collecting Doppler spectra with spatiotemporal resolutions similar to KASPR (Table 1) and located next to KASPR, which allows good beam matching and reliable DWR measurements. The data during the cases were collected every four seconds at 30-m vertical spacing with a beamwidth of 0.3° (Table 1).

2.3. Micro Rain Radar Pro (MRRPro)

265

The MRRPro is the latest version of the MRR developed by Metek GmbH that has evolved to be a powerful standalone profiler for investigations of precipitation and cloud dynamics with very low installation and logistics effort. The MRRPro features a high-performance processing unit which significantly improves the options in the operating parameters (Table 1). During the observation in this study, the MRRPro collected Doppler spectra at a 60 m range-gate spacing every four seconds up to the maximum observation range of 7 km. The Nyquist velocity was 12.08 m s^{-1} during the observations producing the velocity bin spacing of 0.192 m s^{-1} .

270

2.4. Ground-based in-situ measurements

275

A Parsivel optical disdrometer measures terminal velocity and horizontal size of individual precipitation particles passing through a sheet of light (30-mm wide, 1-mm high, and 180-mm long) with a 650-nm laser diode with a power of 3 mW (Löffler-Mang and Blahak, 2001). The total measuring surface has an area of 54 cm^2 . The measured size and velocity are classified into one of 32 size bins ranging from 0.062 to 24.5 mm and 32 velocity bins ranging from 0.04 to 20.5 m s^{-1} every 1 minute.

280

285

The Multi-Angle Snowflake Camera (MASC) is located adjacent to the Parsivel. The MASC consists of three cameras that are separated by an angle of 36° , each pointed towards the focal point about 10 cm away (Garrett et al., 2012; 2014). On top of each camera rests a 2700 lumen light emitting diode. The focal point lies within a ring that has two near-infrared-emitter-detector-pairs arranged in arrays that are separated vertically by 32 mm. The arrangement of the emitter-detector pairs allows for a trigger depth of field of 3100 mm^2 but because of the camera field of view and depth of focus, only about 11% of the images taken are in focus. Falling hydrometeors larger than 0.1 mm are recorded and their fall speed is calculated as the time difference between triggering each emitter-detector pair.

290

Table 1: Specifications for KASPR, ROGER, and MRRPro.

	Ka-band Scanning polarimetric radar (KASPR)	W-band profiling radar (ROGER)	Micro Rain Radar Pro (MRRPro)
Frequency	35.29 GHz (wavelength $\sim 8.5 \text{ mm}$)	94.8 GHz (wavelength $\sim 3.2 \text{ mm}$)	24.23 GHz (wavelength $\sim 12.4 \text{ mm}$)
Range resolution	configurable between 15 – 200 m; 15 m in VPT, 30 m in RHI and PPI for this study	5 – 150 m, 30 m for this study	> 10 m, 60 m for this study
Beam width	0.32°	0.3°	1.5°
Maximum range	Configurable; 15 km in VPT, 30 km in RHI and PPI for this study	Configurable; 18.5 km for this study	Configurable; 7 km for this study



Velocity resolution	Configurable; 0.04 m s ⁻¹ for this study	Configurable; 0.08 m s ⁻¹ for this study	Configurable between 0.05 – 6.00 m s ⁻¹ for this study
Observables	Reflectivity, Doppler velocity, full set of polarimetric variables, Doppler spectra	Reflectivity, Doppler velocity, Doppler spectra	Reflectivity, Doppler velocity, Doppler spectra

295 3. Method

3.1. Reflectivity calibration and DWR estimation

300 KASPR reflectivity measurements were well calibrated using a corner reflector technique (Lamer et al. 2020). Therefore, systematic offsets for the MRRPro and ROGER total reflectivities have been corrected by comparing them with the KASPR reflectivity at cloud bases from a different non-precipitation cloud case. The MRRPro and ROGER reflectivity and mean Doppler velocity data were interpolated into the KASPR VPT data resolution (15-m range and 1-sec time spacings).

305 Gaseous attenuation needs to be considered and corrected when using short-wavelength radars (Lamer et al., 2021). The MRRPro’s K-band (24 GHz) frequency is the lowest in the present study, however, the 24 GHz frequency is very close to a peak in the water vapor absorption spectrum (e.g., Liebe et al., 1993; Rosenkranz, 1998). Therefore, the water vapor attenuation for MRRPro could also be significant. We corrected the MRRPro, KASPR, and ROGER reflectivities for water
 310 vapor attenuation based on the Rosenkranz (1998) results, using sounding profiles launched twice daily (00 and 12 Z) at Upton, 21 km east of the observatory. The estimated column-integrated two-way attenuations at K, Ka, and W bands for our case study were up to 0.7, 0.2, and 1.2 dB, respectively.

315 Another source of the gaseous attenuation we should consider is oxygen (e.g., Liebe et al., 1993). Although the attenuation in oxygen may not be as large as that in water vapor, it may be non-negligible. We also estimated the attenuation by oxygen (i.e., dry air) for each of the three frequencies using the sounding profiles and corrected the MRRPro, KASPR, and ROGER reflectivities. The estimated column-integrated two-way attenuations for dry air at K, Ka, and W
 320 bands were generally 0.1, 0.2, and 0.3 dB, respectively.

Liquid water, which was expected to be present in precipitating clouds as supercooled droplets producing riming can also be a cause of significant attenuation. Riming commonly occurs in
 325 snowstorms observed along the U.S. North East Coast indicating the presence of significant amounts of supercooled cloud water in the snowstorms (e.g., Colle et al., 2014). However, it was difficult to identify liquid cloud layers and liquid water content and estimate specific attenuation at each range bin in the ice clouds. Moreover, attenuation by ice particles might be significant if the large amount of ice were produced in the clouds and the radar beam passed through the ice layers. Tridon et al. (2020) proposed a relative path-integrated attenuation (PIA) technique to
 330 retrieve liquid-water content using DWR profiles. A key idea of this technique is that the DWR from dual frequency radars near cloud tops, where it is expected that small ice crystals are in the Rayleigh scattering regime for both radar wavelengths, is mainly due to the PIA associated with liquid cloud droplets and ice particles. The DWR attributed to the total attenuation should then be equal to the DWR plateau near the cloud top. We applied the Tridon’s et al. (2020) technique



- 335 to the DWR from KASPR and ROGER measurements to find DWR plateau near the cloud top
with the following adaptations:
- the measured DWR_{KaW} are averaged over 450 m (30 gates) and 20 seconds (20 rays).
 - The DWR variance within the moving windows defined above must be lower than 4 dB^2
 - 340 • KASPR reflectivity and its variance (within the same moving windows) must be lower
than 5 dBZ and 2.5 dB^2 , respectively.
 - the DWR plateau is found where the DWR gradient is lower than 1 dB km^{-1} near the
cloud top at each profile.
 - the masked DWR_{KaW} is averaged at the cloud-top layer, and the DWR value is considered
 - 345 the total PIA.

The ROGER reflectivity was corrected for the estimated PIA linearly in the cloud layer from the
ice cloud base, so that the total attenuation in the column was consistent with the estimated PIA.
This assumption might produce an uncertainty, however, this kind of correction showed reasonable
350 results compared to no correction for PIA, as demonstrated by previous studies (e.g., Dias Neto
et al., 2019; Oue et al., 2018). The DWR plateau-based PIA estimation technique requires enough
sensitivity to capture cloud tops where Rayleigh scattering is expected for both. The MRRPro is
sufficiently sensitive to precipitation (Fig. 4c) but not to small particles with reflectivity $< 0 \text{ dBZ}$.
355 The MRRPro reflectivity near its echo top could still include non-Rayleigh scatterings at Ka or W
bands. Because of this, attenuations by hydrometeors in the KASPR and MRRPro reflectivity
fields were not accounted for using the DWR plateau-based attenuation correction in this study.
Moreover, the presence of supercooled liquid droplets might cause total signal extinction. A
microwave radiometer deployed at the SBRO observed liquid water path (LWP) values, which
360 were generally around 150 g m^{-2} before the precipitation onset. According to Tridon et al. (2020),
this amount of liquid should produce a path integrated attenuation less than 1 dB in the KASPR
and MRRPro reflectivity measurements.

Another error source of the DWR analysis is radar beam mismatching. The three radars were
located at the same observation site; the distance between those radars were less than 5 m ,
365 therefore, we expect that the beam mismatch due to location is small. On the other hand, a
difference in beamwidths (Table 1) is another possible cause of beam mismatching. The KASPR
and ROGER beamwidths are well matched, while MRRPro's beamwidth is 5 times larger than
those of the KASPR and ROGER. The beamwidth differences between MRRPro and KASPR, and
MRRPro and ROGER might result in larger variabilities of DWRs.

370

3.2. Mean Doppler velocity

Similar to the reflectivity measurements, the MRRPro and ROGER mean Doppler velocity data
375 were interpolated into the KASPR VPT data resolution. The observed mean Doppler velocities
from the 3 radars were corrected for air density changes based on the sounding profiles and
adjusted to the surface.

380 3.3. KASPR polarimetric observables



385 The polarimetric radar observables such as Z_{DR} and K_{DP} are more prominent when they are
collected at lower elevation scans, whereas the DWR data were collected by vertically pointing
measurements. To compare those two data sets from the different types of scans, we employed a
quasi-vertical profile (QVP) technique proposed by Ryzhkov et al. (2016). The QVP technique
azimuthally averages polarimetric radar variables for each conical PPI scan at non-zero elevations
to produce these variables in a height versus time format. The QVPs have high vertical resolutions
allowing for capture important polarimetric radar signatures and their evolution (e.g., Griffin et
al., 2018; 2020; Kumjian and Lombardo, 2017; Troemel et al., 2019). We use the PPI scans at an
390 elevation angle of 15° every 7-8 min with a scan rate of 6° s^{-1} . Since the slant range resolution of
the 15° PPI data is 30 m, the corresponding QVP data have the vertical spacing of approximately
10 m and the maximum height of 7.8 km. Note that the actual vertical resolution of QVP is
determined by the vertical size of the radar resolution volume, which increases with distance from
the radar (Ryzhkov et al., 2016). The use of conical PPI at a higher elevation angle (15°) for QVP
395 reconstruction ensures relatively high horizontal resolution at lower altitudes (11 km at the height
of 2 km) that facilitates direct comparison with the DWR profiles from the three radar vertically
pointing measurements. The KASPR QVP data were interpolated into the KASPR VPT data
resolution, similar to Oue et al. (2018). Because a single PPI scan was performed every 7 min
while the KASPR 5-min VPT dwell collecting profile data every second was performed in a 15-
400 min interval, a single KASPR QVP corresponds to about 150 DWR profiles.

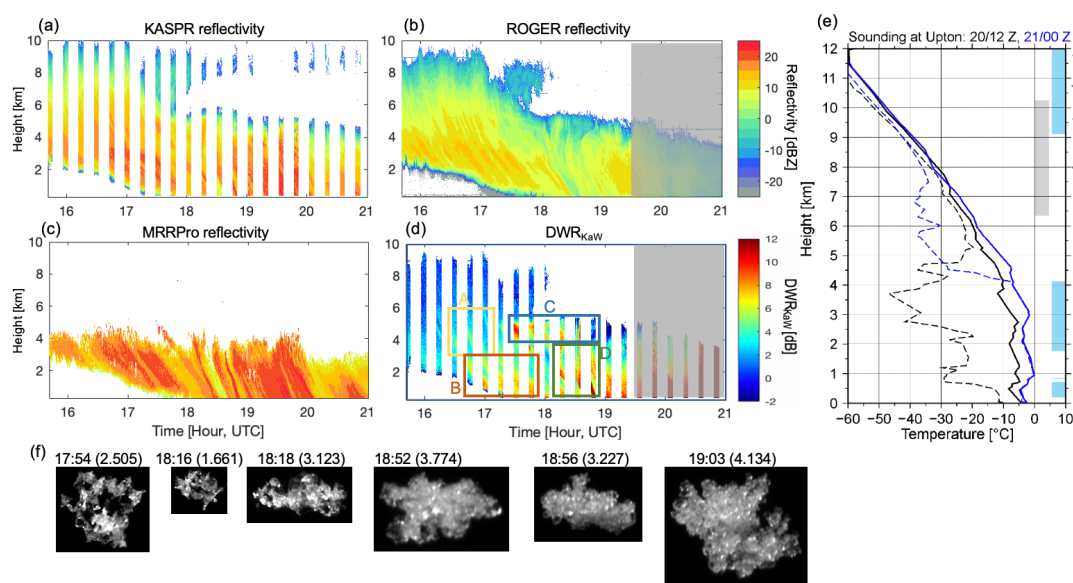
4. Case Description

405 During the 2018-2019 and 2019-2020 winter seasons, most of precipitation was non-dry snow
including rain, wet snow, refrozen particles, and sleet, and provided very few dry snow events at
the ground around Long Island, NY. Those non-dry snow particles caused significant attenuation
of radar signals particularly at millimeter wavelengths and accumulation on the radomes. Although
the majority of the observed precipitation cases during the winter seasons included the non-dry
410 snow particles near the ground, for a few cases before snow started to accumulate, ice clouds (with,
possibly, embedded supercooled cloud layers) were observed aloft. We selected a period from a
snow precipitation case on February 20, 2019, when KASPR VPT, ROGER, and MRRPro
simultaneously observed snowfall without significant attenuations.

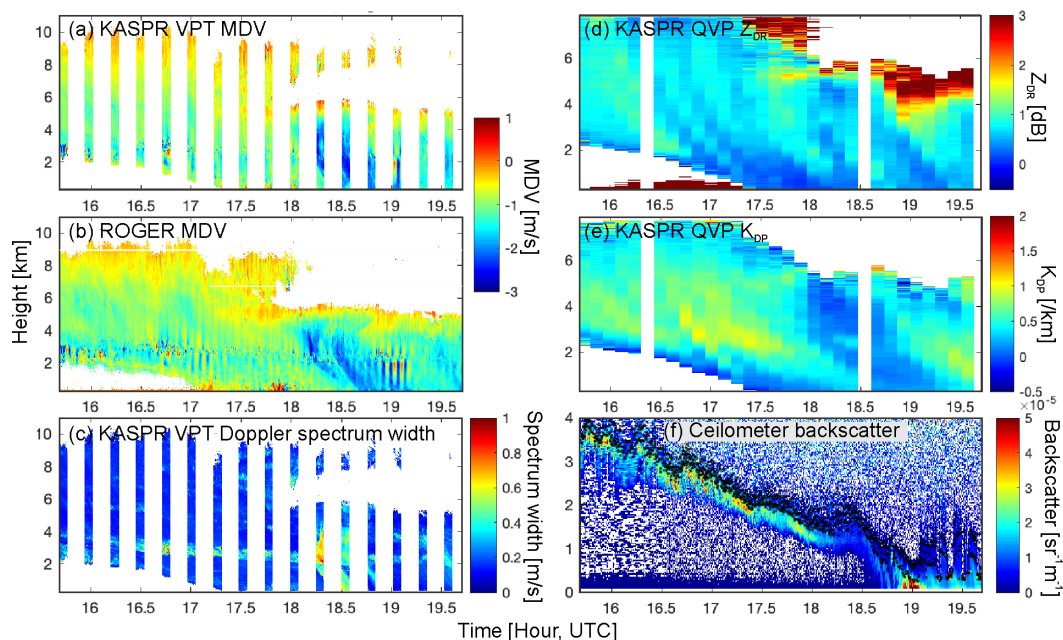
415 A high pressure system at the surface persisted around Long Island from 09 UTC to 21 UTC on
February 20, 2019, while two troughs were also identified to the southeast of Long Island: one was
elongated from a low pressure system in Tennessee to Pennsylvania, and the other was associated
with another low pressure system around the coast of Georgia and lay along the East Coast toward
Long Island. Either one of the two or both could be accompanied by a warm frontal-like stratiform
420 precipitation providing snow in Long Island. Snow precipitation started at around 18:00 UTC at
SBRO. Based on the MASC-observed particle images and Parsivel-observed particle diameter and
fall velocity, dry snow aggregates dominated from the beginning till 23:30 UTC, and then the
dominant precipitation included mixed-phase particles and changed into pure rain at around 04:00
425 UTC on February 21.



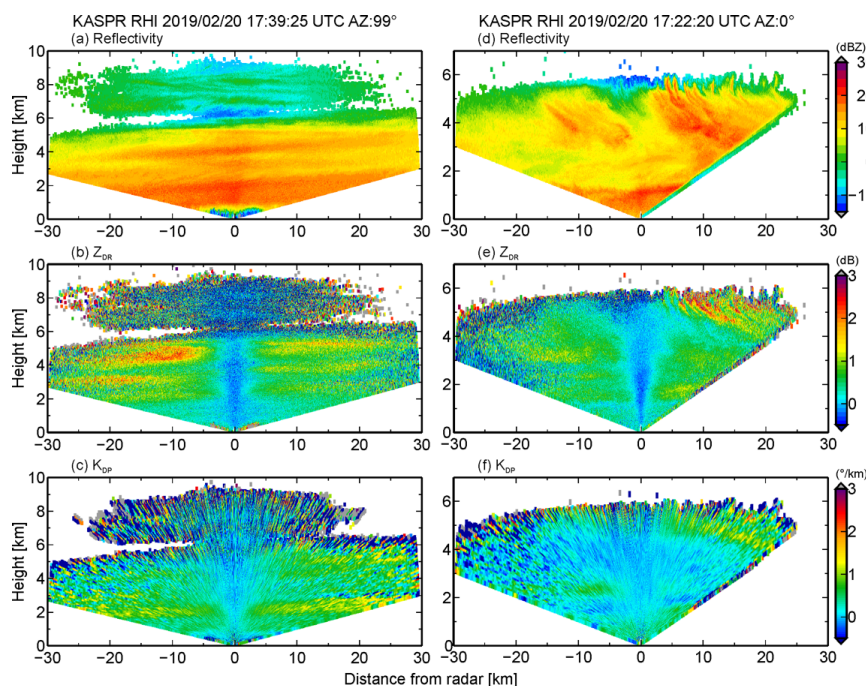
430 Figures 4 and 5 show the time-height curtain images of the reflectivities from the three radars and KASPR and ROGER MDV together with KASPR polarimetric QVPs. The triple frequency measurements started at 15:41 UTC. The cloud base descended until the lidar backscatter signal reached the KASPR's lowest gate (0.4 km altitude) at 19:00 UTC. The cloud top attained 10 km altitude, but the cloud top was decoupled from the ice precipitation since 17:45 UTC.



435 Figure 4: Height-time cross sections of (a) KASPR VPT reflectivity, (c) ROGER reflectivity, (b)
 440 MRRPro reflectivity, and (d) DWR of KASPR reflectivity to ROGER reflectivity on Feb. 20,
 2020, (e) vertical profiles of temperature (solid line) and dew point temperature (dashed line)
 from the NWS Upton sounding measurements at 12 UTC on Feb. 20 (black color) and 00 UTC
 on Feb. 21 (blue color), 2020, and (f) examples of snowflake images captured by MASC. Boxes
 in (d) represent analysis regions used for Figs. 7-10. Gray and blue shades in (e) represent
 440 regions of supersaturation with respect to ice for 12 UTC on Feb. 20 and 00 UTC on Feb. 21,
 respectively. Each image in (f) displays observation time and maximum dimension in parenthesis
 (unit is mm).



445 Figure 5: Height-time cross sections of (a) MDV from the KASPR VPT measurements, (b) MDV from the ROGER measurements, (c) spectrum width from the KASPR VPT measurements, (d) QVP of KASPR Z_{DR} , (e) QVP of KASPR K_{DP} , and (f) ceilometer backscatter on Feb. 20, 2020. Black dots in (f) represent cloud base heights.



450



Figure 6: KASPR (a,d) reflectivity, (b,e) Z_{DR} , and (c,f) K_{DP} from RHI measurements (a,b,c) at 17:39 UTC at an azimuth angle of 99° and (d,e,f) at 18:22 UTC at an azimuth angle of 0° .

455 The KASPR and ROGER reflectivity fields indicated generating cell-like features by 17:10 UTC
near the cloud top above 8 km altitude (Fig. 4), as the MDV indicated convection features in the
generating cells (Fig. 5). These generating cells produced fallstreaks underneath as reflectivity
increased toward the ground and reached the ground by 18:20 UTC. KASPR RHI scans in Fig. 6
460 showed fallstreaks elongating from the generating cell layer following the wind direction above
the 2 km altitude (W-E direction). The KASPR Z_{DR} was enhanced between the fallstreaks while
 K_{DP} increased in the lower part of the enhanced Z_{DR} layer and just below the enhanced Z_{DR} layer.
The enhancement of Z_{DR} generated at a height of 5-6 km, where the temperature was ranging from
-20°C to -15°C corresponding to a dendritic growth layer and close to supersaturation with respect
465 to ice from the 12 UTC sounding (Fig. 4e). This is a typical signature of the aggregation and
generation of dendritic crystals commonly observed by previous studies (e.g., Kennedy and
Rutledge, 2011; Schneebeli et al., 2013; Kumjian et al., 2014; Williams et al., 2015; Oue et al.
2018). The DWR_{KaW} increased toward the ground in the fallstreaks, as reflectivity increased. At
times corresponding to the fallstreaks reaching the ground, MASC observed large aggregates.

470 Starting from 17:50 UTC, precipitation observed at the surface originated at 6 km altitude. The
KASPR RHI measurements revealed that cloud aloft was decoupled from below and there were
structured generating cells near the lower cloud top at 6 km (Fig. 6). Large Z_{DR} values were
observed between the generating cells and between fallstreaks, while K_{DP} slightly increased just
below the generating cell layer but decreased to near zero within the fallstreaks. There was a layer
475 of large DWR_{KaW} at 4-5.5 km altitude from 17:15 to 18:50 UTC, even though the Ka-band
reflectivity was smaller than that in the former fallstreaks. The large DWR_{KaW} extended toward
the ground and reached the surface at 18:30 UTC (Fig. 4d), as the KASPR polarimetric signatures
associated with the fallstreaks reached the surface (Figs. 5d and 5e). Corresponding to the time
when the fallstreak features reached the surface, MASC observed rimed particles (Fig. 4f). These
480 DWR and polarimetric features likely indicate an ice particle growth, however, it is hard to
determine specific ice growth processes (i.e., distinguishing riming and aggregation processes)
from the DWR_{KaW} or the polarimetric observables only.

There are several signatures that suggest different types of ice particle growth during the two
485 periods. A distinct difference between the two periods is found in the MDV from the vertically-
pointing measurements and the KASPR polarimetric observables; they suggest different ice
particle fall speeds attributed to the particle types and microphysics. The downward motion within
the fallstreaks during the first period gradually increased toward the ground to 1.5 m s^{-1} , indicative
of growth of individual ice particles. The fallstreaks corresponded to the enhanced K_{DP} , but
490 decreased Z_{DR} , suggesting that oblate small particles aggregated within the fall streaks. In contrast,
the latter period corresponded to decreased K_{DP} , while Z_{DR} values are enhanced near the 6 km
altitude but decreased toward the surface. These K_{DP} and Z_{DR} evolutions suggest that small oblate
ice crystals formed at 6 km altitude and aggregated as they fell forming spherical shapes, as many
previous polarimetric radar studies observed. The MDV showed faster downward motion
495 compared to the fallstreaks in the first period, suggesting heavy aggregation and/or riming.



Another interesting characteristic to be noted is that there was a distinct region of turbulence, which can clearly be seen as a layer with large spectrum width and variability of MDV at around 3 km altitude. This was consistent with large lidar backscatter values suggesting liquid cloud base. The reflectivity and DWR of fall streaks were intensified below the turbulence layer.

Although the individual radar parameters suggest a variety of ice particle types and microphysical processes, it is not straightforward to identify the ice particle types and distinguish the processes, in particular aggregation and riming, by a single measurement.

5. Results and Discussions

5.1. DWRs from the three frequencies

Based on the DWR_{KaW} height-time plots, we selected four regions as shown in Fig. 4d, each of which had similar DWRs, MDV, and polarimetry features to identify ice particle types and their growth processes. We first present traditional triple-frequency DWR-DWR diagrams (DWR_{KW} versus DWR_{KKa} in Fig. 7) for each selected region. The DWRs from Region A and Region B tend to be distributed toward the model low rime degree lines (larger DWR_{KKa} at a given DWR_{KW}), while those from Region C and Region D were distributed toward the higher rime degree regions (smaller DWR_{KKa} at a given DWR_{KW}). These are consistent with MASC ice particle observations. Although the distribution of the DWRs for each region seems to be significantly separated, most of the data are overlapped, making it hard to distinguish the growth processes and types. This is, in part, because K-band (24 GHz) and Ka-band (35 GHz) measurements are not sufficiently separated in the frequency domain.

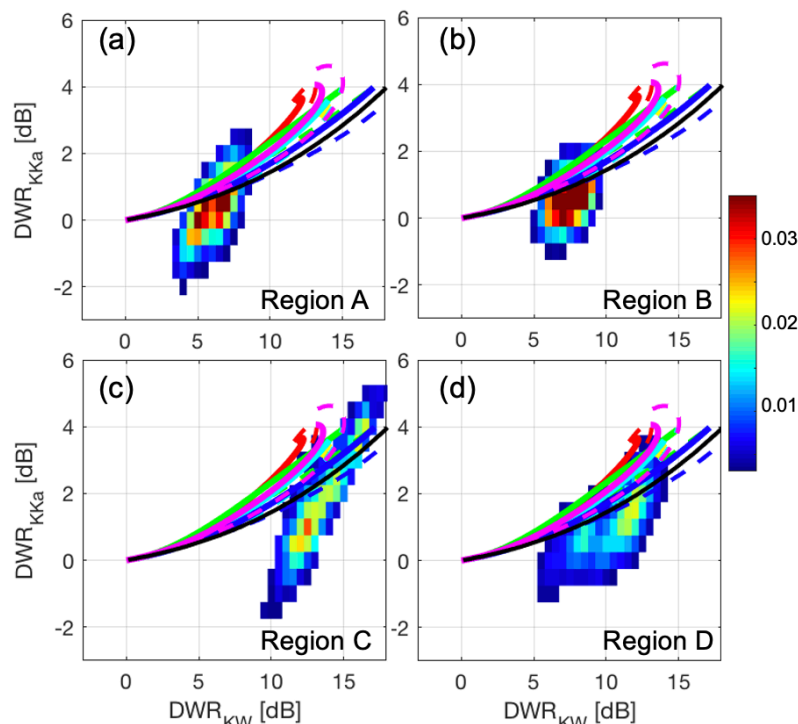
Besides the insufficient frequency separation, there are data points that deviate from the model lines in the DWR_{KW} versus DWR_{KKa} field in each region. There are several causes of such deviations (e.g., Lamer et al., 2020). The most likely cause is unaccounted attenuations particularly at Ka and W bands due to either supercooled cloud water or ice or both. The ceilometer backscatter measurements shown in Fig. 5f, in addition to the MWR LWP measurements, suggest that thin supercooled liquid cloud layers were indeed present at least around the large Doppler spectrum width layer. Unfortunately, the ceilometer backscatter information is insufficient to provide a complete mapping of such layers because of complete signal extinction caused either by the ice clouds or by underlying liquid layers themselves. Ice particles could also cause signal attenuation (Battaglia et al., 2020; Tridon et al., 2020) particularly for the shorter-wavelength radars. Although the DWR plateau-based PIA technique has corrected the ROGER reflectivity for those attenuations related to the KASPR reflectivity (Sect. 3.1), the attenuation in the KASPR reflectivity itself cannot be accounted for in this study. This factor also causes underestimation of the PIA-corrected ROGER reflectivity.

Secondly, the beam mismatch could be significant when the radar beams penetrate narrow, fine fallstreaks, even though the radars were collocated within 5 meters from each other. As mentioned previously, the KASPR and ROGER beamwidths are well matched (0.3°), while the MRRPro's beamwidth is 5-times larger (1.5°). The radar sampling volumes, which are larger at higher altitudes, cannot resolve the small time and spatial scale phenomena, and the difference in



545

beamwidth is a source of uncertainty. Moreover, the ice particle models may not represent all the gamut of ice particles possibly present in the clouds.



550

Figure 7: (a-d) DWR_{KKa} versus DWR_{KW} diagrams for Regions A, B, C, and D, respectively. Color shades represent normalized frequency. Lines in each panel represent the SSRGA calculations using particle type and PSD models described in Sect. 3.4. The color line legend is the same as in Figure 1a, and black lines are same as black lines in Fig. 1b.

5.2. DWRs coupled with MDV and polarimetric variables

555

Observed MDV is attributed to mainly the vertical air motion and the particle fall speeds, which is sensitive to particle size, rime degree, size distribution, and type, and can provide additional information to distinguish ice types and processes. Kneifel and Moisseev (2020) demonstrated that MDV is a function of rime fraction. We further illustrate that MDV coupled with DWR shows a good indicator of degree of riming. Figure 8 shows the observed DWR_{KaW} as a function of KASPR

560

MDV together with the model plot with different rime degrees (lines). Most of DWR_{KaW} values from Region A are less than 7 dB and are located between the middle (yellow and cyan) and low (red and magenta) rime degree lines, suggesting light riming of small aggregates (Fig. 8a). These particles could grow keeping the similar degree of riming by aggregation, as the data points from Region B are shifted toward larger DWR_{KaW} values between the middle and low rime degree lines (Fig. 8b). It is possible that the turbulence layer at around 3 km altitude (Figs. 5b and 5c)

565

contributed to light riming. The turbulence also contributed to the wide distribution of MDV.



DWR_{KaW} from Region C generally follows the low-rime degree particle lines; DWR_{KaW} increased from near zero to 10 dB while MDV changed from near zero to -0.8 m s^{-1} . Some data points are shifted toward the middle-rime degree particle lines (i.e. faster downward motion at a given DWR_{KaW}). These data clusters suggest that the aggregation dominated, but some particles started riming. Region D, which is located below Region C, has also generally two data clusters. A smaller data cluster closely follows the low-rime degree lines, as the DWR_{KaW} increased 2 to 9 dB while the MDV changed from -0.6 m s^{-1} to -1.3 m s^{-1} . The other population, which has higher occurrence, is generally along the middle rime degree lines; the DWR_{KaW} increased from 3 to 12 dB while the MDV changed from -1.8 m s^{-1} to -2.5 m s^{-1} in the middle of the population. The left edge of the second data population is closer to the higher riming degree (blue and green) lines. Those downward MDVs belonging to the two populations are consistent with fall velocities of aggregates and heavily-rimed particles, respectively, studied by Locatelli and Hobbs (1974). These characteristics suggest that aggregates produced near the cloud top at 6 km rimed during the falling as particle fall speeds quickly increased. These distinct separations of the particle populations associated with the particle growth processes are not clearly found in the triple-frequency DWR field in Fig. 7, whereas these are also shown in the DWR_{KW} versus KASPR MDV (Fig. 8e) and DWR_{KKa} versus KASPR MDV (Fig. 8f) diagrams.

585

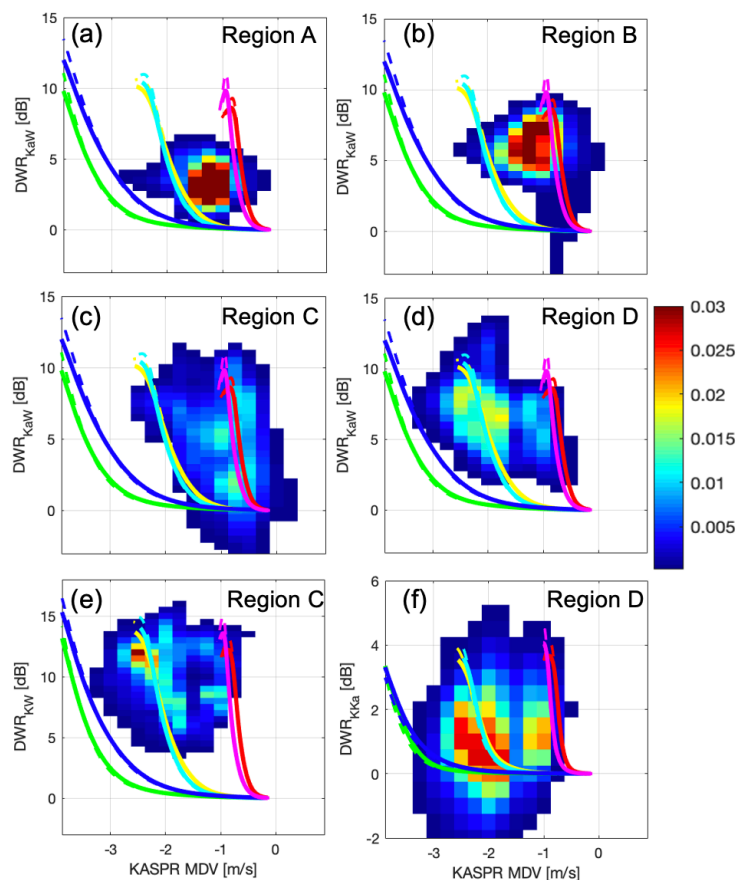




Figure 8: (a-d) KASPR VPT MDV versus DWR_{KaW} diagrams for Regions A, B, C, and D, respectively. (e) KASPR VPT MDV versus DWR_{KW} diagram for Regions D, and (f) KASPR VPT MDV versus DWR_{Kka} diagram for Regions D. Color shades represent normalized frequency. Lines in each panel represent the SSRGA calculations using different particle models and PSDs described in Sect. 3.4. The legend of the lines is same as Figure 1.

Adding polarimetric information supports this interpretation and gives further insights into particle microphysics in terms of their shapes. Figures 9a-d and Figures 9e-h are the same as Figs. 8a-d, respectively, but the color shade represents KASPR QVP Z_{DR} (Figs. 9a-d) and K_{DP} (Figs. 9e-h), respectively. In the data grouping following the low rime degree lines for Region C and Region D, Z_{DR} values decreased as DWR increased (Figs. 9c,d), while K_{DP} values slightly decreased by approximately $0.2 \text{ } ^\circ \text{ km}^{-1}$ (Figs. 9g,h). It can be interpreted that small ice particles producing near zero DWRs were horizontally-oriented oblate particles in the dendritic crystal growth zone (temperature of -15 to -10°C), which produced large Z_{DR} values and then aggregated to be large size as DWR increased. On the other hand, individual frequency pair DWR for vertically pointing measurements also strongly depends on particle aspect ratios (Matrosov et al. 2019). The impacts of particle aspect ratio on DWR_{KaW} values could be as high as ~ 3 and ~ 5 dB for particle distributions with median volume size of 1 and 2 mm, respectively (Matrosov 2021). The increase of DWR_{KaW} in the diagrams can include both the particle size and shape effects.

The DWR-MDV diagrams suggest that as DWR_{KaW} increased, the MDV corresponding to the low rime degree particle populations in both Region C and Region D reached $\sim 1 \text{ m s}^{-1}$, consistent with the fall speeds of low rime degree aggregates. This effect is more likely due to the increase of size rather than aspect ratio. During the aggregation process, the size distribution of snowflakes evolves in such a way that the concentration of smaller, higher-density particles decreases whereas the number of larger, lower density snowflakes increases. This is a primary reason for the reduction of both Z_{DR} and K_{DP} due to aggregation, although the increase of the average aspect ratio and possibly more chaotic orientation additionally contribute to such a reduction. The K_{DP} values could also be accounted for by changes in the number concentration of the horizontally-oriented oblate particles (with aspect ratio < 1); its increase contributes to increasing K_{DP} .

In the DWR-MDV data clusters following the high-rime degree particle lines in Region C, Z_{DR} and K_{DP} quickly decreased as the DWR_{KaW} and the magnitude of MDV increased; Z_{DR} values decreased from 2 dB to 0.5 dB, and the K_{DP} values decreased from $0.4 \text{ } ^\circ \text{ km}^{-1}$ to near zero (Figs. 9c,g). Although the increase of the DWR_{KaW} includes the effects of both size and aspect ratio as discussed above, the increase of the magnitude of MDV can represent the increase of size. The Z_{DR} and K_{DP} values are lower than those from the cluster along the low-rime degree models at a given DWR_{KaW} . Lower K_{DP} and Z_{DR} values suggest a particle growth by heavier riming, which tend to produce more spherical particles.

These Z_{DR} and K_{DP} characteristics shown in both low and high rime degree particle data groups in Region C are very similar to those in Region D, but the K_{DP} and Z_{DR} values in Region D are generally lower at a given DWR_{KaW} , with a mean MDV of -3.5 m s^{-1} (Figs. 9d,h). The lower K_{DP} and Z_{DR} in Region D represent further particle growth which is accompanied by the decrease of their density, increase of their aspect ratios, and more random orientation.



It is interesting that for DWR_{KaW} values less than 5 dB in Region C, the observed Z_{DR} values with faster fall speeds (corresponding to the high-rime degree particle lines) are larger than those with slower fall speeds (corresponding to the low-rime degree particle lines) at a given DWR_{KaW} (Fig. 9c). This suggests that riming first worked to fill the gaps of branches of dendrite crystals, resulting in increasing the mass of individual crystals without significant change in their aspect ratio and thus Z_{DR} increased. This type of riming would not significantly contribute to the increase of K_{DP} (Fig. 9g), likely due to low concentration of such particles. This characteristic is consistent with the early stage of riming reported by previous studies (e.g., Oue et al., 2016; Li et al., 2018).

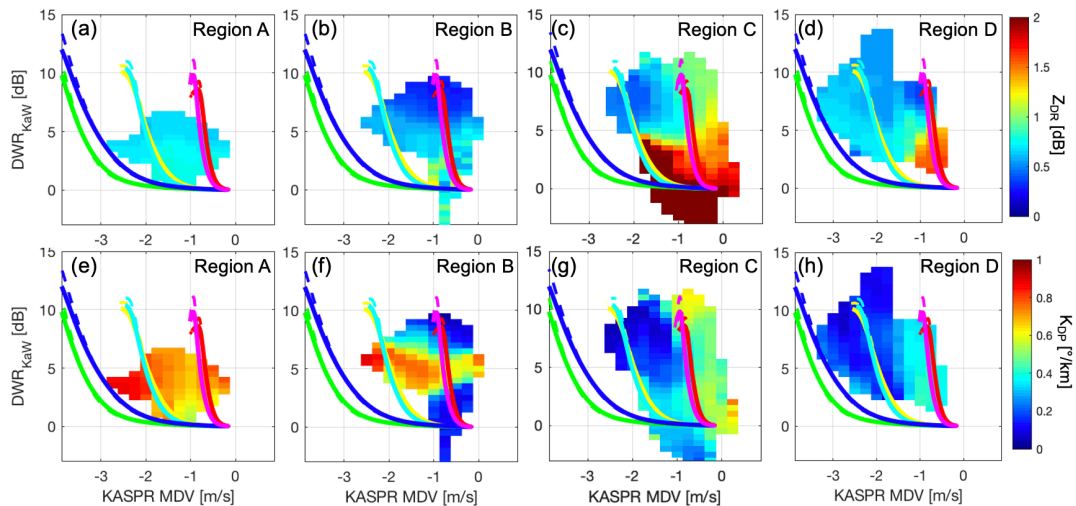


Figure 9: KASPR VPT MDV versus DWR_{KaW} diagrams for (a,e) Region A and (b,f) Region B, (c,g) Region C, and (d,h) Region D. Color shades in (a-d) and (e-h) represent KASPR QVP Z_{DR} and K_{DP} , respectively, averaged at each MDV- DWR bin. Lines in each panel represent the SSRGA calculations using particle type and PSD models described in Sect. 3.4. The legend of the lines is the same as in Figure 1.

Compared to Region C and Region D, the polarimetric observables in Region A and Region B (Figs. 9 a-b and Figs. 9e-f) do not show clear trends with changes of rime degree, and the dynamical oscillation shown in Figs. 5a-c results in an uncertainty in the particle identification for Region A, particularly when DWR_{KaW} values are smaller than 5 dB and MDV is varying between -3 and 0 m s^{-1} . Adding polarimetric variables together with temperature information facilitates the interpretation of the microphysics. Z_{DR} values in Region A are positive, but smaller than 1 dB, and smaller than those from the later fallstreaks (Region C and Region D, for a given DWR), suggesting an aggregation process which was accompanied by a decrease of particle density, an increase of their aspect ratios, and more random particle orientations compared to Region C and Region D. In contrast, K_{DP} is larger than that from the later fallstreaks. The large K_{DP} and smaller Z_{DR} values in Region A suggest aggregation intensified by higher number concentration of ice crystals. The increase of ice number concentration can be explained by two processes. One possible cause is that near the dendrite growth regime (around -15°C), dendritic ice crystals were nucleated. The dendritic branches could work to facilitate interlocking (Pruppacher and Klett, 2010). This is



665 a well-known characteristic in winterstorms reported by many previous studies using polarimetric
radar measurements (e.g., Kennedy and Rutledge, 2011). Another process is seeding from above
(e.g., Griffin et al, 2018; Oue et al. 2018), which is more likely to contribute to the increase of ice
concentration for this case. The cloud top height during observations in Region A and Region B
reached 10 km, approximately 4-km higher than in Region C and Region D (Figs. 5 and 6). This
fact suggests that higher concentration of ice particles aloft seeded in Region A. Moreover, a
670 possible light riming in the turbulence region could increase the mass of individual particles, hence
 K_{DP} , as the cluster extended to the middle rime degree included large K_{DP} values.

The particles were further growing at lower altitudes as DWR_{KaW} increased with decreasing Z_{DR}
in Region B. However, a sublimation process near the ground could also be plausible. The nearest
675 soundings at Upton (12 Z, black lines in Fig. 4e) showed a dry air condition at the lower altitudes.
This sounding time was ~5-6 hours before the radar observation, but the dry air condition could
still be present near the ground, thus favouring sublimation in the lower altitudes of Region B. Due
to sublimation some branches and/or edges of aggregate particles could have disappeared, resulting
in decreasing the mean volume diameter. The classical aggregation process could have stopped
680 with K_{DP} remaining relatively large because it usually decreases proportionally to the mean volume
diameter. Decrease of IWC attributed to the sublimation might have been minor with any
noticeable impact on K_{DP} . These processes related to the sublimation are represented by a cluster
with high K_{DP} in Region B, where the DWR_{KaW} values slightly increased while K_{DP} values kept
high compared to Region A. The sublimation also contributed to decreasing particle fall speed, as
685 shown by a minor decrease of the magnitude of MDV in the data group, but the MDV probably
resulted from some balance between the fall speed increase due to aggregation and its decrease
due to sublimation. The classical diabatic sublimation cools and moistens the ambient air.
Therefore, the sublimation subsided as the cloud base descended with time (Fig. 5f) and snow
particles in the fallstreaks eventually reached the ground.

690

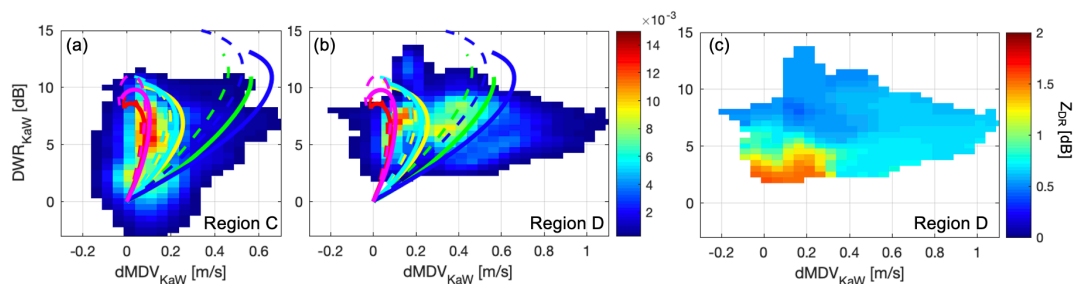
5.3. DWR coupled with differential MDV

The MDV measurements also have frequency dependencies because of the complex interplay
695 between non-Rayleigh effects and the PSDs. Figure 10 shows dependencies of the ice particle
types on the DWR_{KaW} versus differential MDV ($dMDV = KASPR\ MDV - ROGER\ MDV$)
diagrams for Region C and Region D, together with the scattering calculations using the particle
models. Similar to the DWR-MDV diagram in Fig. 9, Region C includes a cluster with a higher
number of occurrences along the low-to-middle rime degree particle lines, and a lower frequency
700 cluster extends toward the high-rime degree particle lines. Region D has more data points for the
high-rime degree particle population.

Region D also includes large $dMDV$ values greater than $0.6\ m\ s^{-1}$ for DWR_{KaW} values between 3
and 10 dB (Fig. 10b). It is possible that the larger values of $dMDV$ correspond to an increase in
705 the particle sizes and not to changes in the degree of riming. The Z_{DR} values corresponding to these
large $dMDV$ values (Fig. 10c) are approximately 0.7 dB, suggesting that the particles were non-
spherical, possibly contributing to the decrease of DWR_{KaW} compared to the spherical particles.



710 As the scattering calculations show, distinguishing among different degrees of riming requires
accurate measurements of MDV with an error of few hundredths of 1 m s^{-1} and exact range-time-
bin gate matching for lower $\text{DWR}_{\text{KaW}} (< 5 \text{ dB})$. Although the vertical air motion contributions in
MDV from each radar are cancelled out in dMDV, subgrid scale turbulence, the wide range of
715 particle fall speeds, and different sampling times for the observations (1 s for KASPR VPT and 4
s for ROGER) can all be sources of uncertainties. This limitation may affect the scatterplot
distributions, e.g. with some points clustering outside the envelop of the model's lines. This
limitation also affects Region A (not shown).



720 Figure 10: Difference of KASPR VPT MDV and ROGER MDV versus DWR_{KaW} diagrams for (a)
Region C and (b) Region D. Color shades represent normalized frequency. (c) is the same as (b),
but the color shade represents KASPR QVP Z_{DR} . Lines in (a) and (b) panels represent the SSRGA
calculations using particle type and PSD models described in Sect. 3.4. The legend of the lines is
725 the same as Figure 1.

5.4. Evaluation using ground-based in-situ measurements

730 The particle properties retrieved from the ground-based measurements including fall speed, size,
aspect ratio, and area ratio are the result of ice growth processes in the clouds aloft. The Parsivel
and MASC observations allowed us to evaluate the radar-based particle characteristics described
above. The Parsivel and MASC collocated with the radars collected precipitation particles after
18:13 UTC and 18:16 UTC, respectively. The snow images from MASC were quantified by
735 measurements of aspect ratio and area ratio, and their time series were presented in Fig. 11. Figures
11a and 11b present frequencies (color shade) together with median values (black line) observed
for a 20-min time range every 1 minute.

740 We also estimated mass-weighted mean diameter for Parsivel-measured PSD. The ice particle
mass was estimated using a methodology proposed by von Lerber et al. (2017). The methodology
is based on a theory that individual particle mass can be expressed based on a hydrodynamic theory
derived by Böhm (1989) using the Reynold's number and the Best number (e.g., Mitchell, 1996;
745 Mitchell and Heymsfield, 2005; Heymsfield and Westbrook, 2010). The equation of mass (Eq. 5
of von Lerber et al., 2017) indicates that the mass can be a function of fall velocity, area ratio, and
size. In the present study, the area ratio is derived from the MASC images, and the fall velocity
and size are estimated from the Parsivel measurements. The Parsivel-observed particle diameter
and fall speed are fitted to a form of $V = aD^b$ where a and b are constants using the 20-min

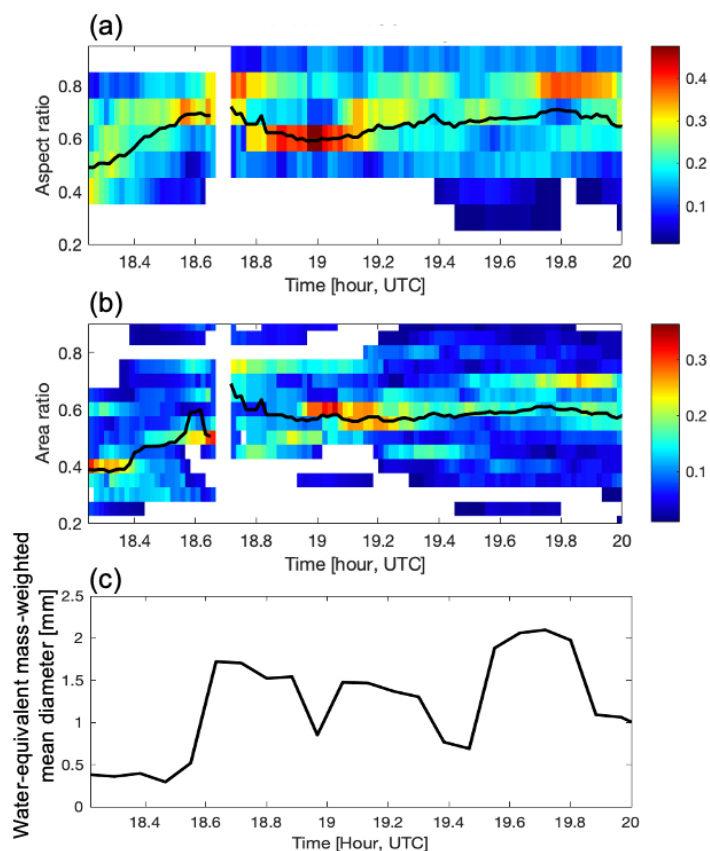


integrated data. Previous studies pointed out that Parsivel's velocity and even size measurements for snow include large uncertainties owing to the sampling limitation (Battaglia et al. 2010). Before estimating the relationships, we removed unrealistic velocity values as follows: 1) data having a small diameter (<1 mm) and too large velocity (>1.5 m s⁻¹) according to Locatelli and Hobbs (1974), and 2) data outside upper and lower boundaries of the V-D relationships. The upper boundary was determined based on Locatelli and Hobbs's (1974) V-D relationships for rimed aggregates, and the lower boundary was determined based on Szyrmer and Zawadzki's (2010) V-D relationships for unrimed aggregates. The Parsivel-measured size was adjusted to the maximum dimension using a technique proposed by von Lerber et al. (2017). Figure 11c presents the time series of the estimated water-equivalent mass-weighted mean diameter from the Parsivel-measured PSD.

These time series are consistent with the fallstreaks reaching the ground. Aspect ratio represents oblateness of particles relating to Z_{DR} and partly contributing to K_{DP} . Korolev and Isaac (2003) and Jian et al. (2017) suggested that mean aspect ratio of observed snowflakes can be around 0.6 or a bit smaller, while that of heavy-rimmed particles such as graupel increases toward 1. Radar depolarization-based retrievals of snowflake aspect ratios near the ground indicated mean aspect ratios of about 0.4 - 0.5 (e.g., Matrosov et al., 2020). Area ratio in the current study is defined as the ratio of the area of the snowflake, which is found by counting all white pixels in a black and white image, to the area of the circumscribing circle defined by the maximum diameter from MASC. The area ratio increases with riming (von Lerber et al. 2017).

The aspect ratio was relatively low before 18:30 UTC, where the median value was less than 0.6. At the same time, the area ratio was also relatively low, where the median area ratio was smaller than 0.5. This period corresponds to time where fall streaks included in Region A and Region B reached near the ground, consistent with the radar MDV-DWR characteristics. The mass-weighted mean size was approximately 0.4 mm, consistent with the scattering model calculations shown in Fig. 2a. It should be noted also that aspect ratio estimates from in situ data (e.g., from Parsivel and/or MASC measurements) are inferred from 2D particles projections, so these estimates usually overestimate actual aspect ratios, which are defined as true minor-to-major particle dimension ratios (Jiang et al., 2017; Matrosov et al., 2017).

The median in situ aspect ratio exceeded 0.6 between 18:30 and 19:00 UTC, while area ratio also increased. The water-equivalent mass-weighted mean diameter increased after 18:33 UTC, as it exceeded 1.3 mm between 18:38 and 19:48 UTC except 18:58, 19:22, and 19:28) UTC. Those large diameter periods correspond to times where fall streaks included in Region D reached the ground. The ground-based characteristics suggests that snowflakes were larger aggregates, which heavily rimed having faster fall speeds, consistent with the observed characteristics of the radar MDV-DWR coupled with the polarimetric observable.



790 Figure 11: Time series of (a) aspect ratio and (b) area ratio of snow particles measured by the
MASC and (c) water-equivalent mass-weighted mean size of Parsivel-measured PSDs. Color
shades and black lines in (a,b) represent normalized frequency and median values, respectively,
for snow particles collected during a 15-min window every 1 minute.

795

6. Summary

800 DWRs from triple-frequency measurements are useful to identify ice particle types and processes
as proposed in previous studies. For the technique to be effective the radar frequencies need to
be well separated. This requirement limits applications when using 24, 35, and 94 GHz frequency
radars, like in this study. Despite this limitation, MDV and polarimetric variables can be used
complementarily to identify ice particle types and distinguish among different ice growth
805 processes and even reveal additional microphysical details.



We conducted triple frequency measurements using the MRRPro (24 GHz), the Ka-band scanning polarimetric radar (KASPR, 35 GHz), and the W-band profiling radar (ROGER, 94 GHz) at the Stony Brook University Radar Observatory in the winter season of 2019-2020. We successfully collected the triple frequency data from vertically-pointing measurements for a snowstorm along the U.S. North East coast on February 20, 2019. Quasi-vertical profile (QVP) height-versus-time data were also obtained from KASPR PPI scans at an elevation angle of 15°. We investigated all pairs of DWR from the triple frequencies (i.e., DWR_{KKa} , DWR_{KW} , and DWR_{KaW}) in conjunction with MDV from the KASPR vertically-pointing measurements and Z_{DR} and K_{DP} from the KASPR QVPs. Overall, it was challenging to discern the precipitation particle types in the DWR_{KKa} -versus- DWR_{KW} diagram only, likely due to insufficient separation of the K-band frequency from Ka band, whereas the DWR-versus-MDV diagrams for all DWR pairs exhibited distinct separations of particle populations attributed to different rime degrees and particle growth processes. Figure 12 presents a schematic DWR-MDV-polarimetric variable diagram for this case.

Regions that included fallstreaks were dominated by the aggregation process, where the DWR_{KaW} increased with the magnitude of MDV corresponding to the scattering calculations for low- to middle- rime degree aggregate particles (e.g., marked 1 in Fig. 12). The DWR_{KaW} values further increased at lower altitudes of the fallstreaks as reflectivity increased. Z_{DR} and K_{DP} values were 0.6 dB and $0.8 \text{ }^\circ \text{ km}^{-1}$, respectively. The small Z_{DR} values in the lower region in conjunction with the MDV and Doppler spectrum width measurements suggested further ice growth produced by aggregation. Larger K_{DP} in the fallstreaks represented high number concentration ice particles generated aloft that facilitated aggregation. A possible light riming in a turbulence region could increase the mass of individual particles, hence K_{DP} (e.g., marked 2 in Fig. 12). A sublimation process apparent near the ground at the beginning of precipitation might result in dissipating branches and/or edges of aggregates and decreasing the mean volume diameters. This caused little increase of DWR and kept K_{DP} large.

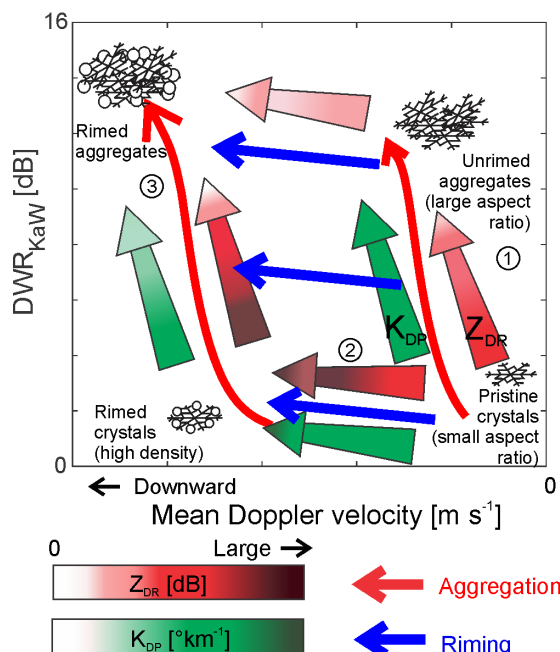
Characteristics of riming were discerned in other regions where several different particle populations were expected. Associated with a population of lower rime aggregates, DWR_{KaW} increased from near zero to 10 dB while the magnitude of MDV increased from near zero to 0.8 m s^{-1} . K_{DP} and Z_{DR} slightly decreased as DWR_{KaW} increased, which were consistent with aggregate particles accompanied by the decrease of their density, increase of their aspect ratios, and more random orientation (e.g., marked 1 in Fig. 12). Another particle population which was expected to have larger degrees of riming was distinguished from the particle populations with smaller degrees of riming using the DWR_{KaW} -versus-MDV diagram (e.g., marked 3 in Fig. 12); it had an increase of DWR_{KaW} similar to that for aggregates with lower riming but the magnitude of MDV was around $2\text{--}2.5 \text{ m s}^{-1}$ (approximately $1\text{--}1.5 \text{ m s}^{-1}$ larger than that for the former particle population). K_{DP} and Z_{DR} rapidly decreased to near zero when DWR_{KaW} increased suggesting a rapid particle growth. Although DWR_{KaW} also strongly depends on particle shape (in addition to dependence on particle size), the increase of the magnitude of MDV was likely attributed to the ice particle growth. In the lower altitudes, the occurrence of the higher rime degree particle populations increased as the magnitude of MDV reached 3.5 m s^{-1} , while K_{DP} and Z_{DR} at a given DWR_{KaW} were smaller as compared to the upper region. These characteristics suggest further riming and increase of aspect ratios. The DWR_{KaW} -MDV diagrams also depicted the early stage of riming where Z_{DR} increased while the magnitude of MDV increased collocated with small increases of DWR_{KaW} and K_{DP} (e.g., marked 2 in Fig. 12). The other DWRs (i.e., DWR_{KKa} and DWR_{KW}) as a function of MDV as well



855 This study illustrated the capabilities of DWR measurements coupled with MDV and polarimetric measurements to discern riming and aggregation processes, which have been often observed by single-frequency radar measurements but not well separated. This approach will improve quantitative estimations of snow amount (i.e., IWC, snow rate) and microphysical quantities such as rime mass fraction (e.g., Moisseev et al., 2017; Li et al., 2018). Dual-frequency measurements

860 coupled with MDV -typically available from all cloud radar systems- not only would be more practical than the triple frequency measurements (since they only involve two radars)) but they are more effective in separating the two processes as well. Such systems, when used in synergy with polarimetric observations, common in research and weather networks (e.g. Kollias et al., 2020a, NWS WSR-88D radars) can reveal complex microphysics as presented in this study. Shorter

865 wavelength radars and lidars as well as microwave radiometers can be complementarily used for better capturing the presence of supercooled liquid droplets and the riming process (e.g., Lamer et al., 2020; Tridon et al., 2020).



870 Figure 12: A schematic DWR-MDV-polarimetric variable diagram based on the observation in this study.



Appendix

875

Calculations of DWR and mean Doppler velocity for aggregated snowflakes using the self-similar Rayleigh-Gans approximation

880 To evaluate the observed DWRs and mean Doppler velocity, we calculated the radar reflectivities
 and mean Doppler velocities at the three frequencies (i.e., 24.0 GHz, 35.5 GHz, and 94.0 GHz)
 using the radar backscattering cross section database obtained from the self-similar Rayleigh–Gans
 approximation (SSRGA) method proposed by Hogan and Westbrook (2014). The SSRGA uses
 the Rayleigh-Gans approximation and its extension for an ensemble of particles, for which
 885 horizontal orientation with no canting was employed. The SSRGA employs simple mathematical
 formulation which is very efficient in the numerical implementation and produces more realistic
 scattering properties compared to spheres/spheroids models, taking into account the internal
 structure of aggregates (e.g., Hogan and Westbrook, 2014; Hogan et al., 2017; Tyynelä et al., 2013;
 Leinonen et al., 2013; Tridon et al., 2019).

890 In this work, the SSRGA was adopted to calculate radar backscattering cross sections at a vertical
 incident angle for individual aggregate particles with different rime degree (i.e. effective liquid
 water path) and size modeled by Leinonen and Szyrmer (2015) and Hogan and Westbrook (2014),
 similar to Tridon et al. (2019). Table A1 lists the particle models with different rime degrees used
 in the present study. To compute the radar reflectivity from the radar backscatter signals from the
 895 database, we used a gamma distribution as a particle size distribution (PSD), where water-
 equivalent mass-weighted diameter (D_m) varied from 0.1 mm to 2.5 mm with a fixed shape
 parameter (μ) of 0 and 4.

900 Mean Doppler velocity at 1000 hPa was computed for each particle model and each PSD using the
 radar backscatter signals and a particle terminal velocity model by Hogan and Westbrook (2014).
 For the all MDV presented in this study, negative values represent downward motions.

Table A1: Particle models used in the present study.

Particle model	Name in figure
Leinonen and Szyrmer (2015) unrimed aggregate model (model A)	LS15A0.0kg/m ²
Leinonen and Szyrmer (2015) rimed aggregate model (model A) with effective liquid water path of 0.5 kg m ⁻²	LS15A0.5kg/m ²
Leinonen and Szyrmer (2015) rimed aggregate model (model A) with effective liquid water path of 2.0 kg m ⁻²	LS15A2.0kg/m ²
Leinonen and Szyrmer (2015) rimed aggregate model (model B) with effective liquid water path of 0.5 kg m ⁻²	LS15B0.5kg/m ²
Leinonen and Szyrmer (2015) rimed aggregate model (model B) with effective liquid water path of 2.0 kg m ⁻²	LS15B2.0kg/m ²
Hogan and Westbrook (2014)	HW14

905

Data availability. The SBRO radar data are available at the SBU Academic Commons.



910 *Author contributions.* Data collection and analysis were made by MO. Conceptualization of the method, interpretation, and writing were shared between MO, PK, SM, AR, and AB. Scattering calculation using SSRGA was made by the AB's group.

Competing interests. The authors declare that they have no conflict of interest.

915

Acknowledgements.

M. Oue, P. Kollias, S. Matrosov, and A.V. Ryzhkov were supported by the National Science Foundation grant # 1841246. A. Battaglia was supported by Atmospheric System Research (grant no. DE-SC0017967). We thank Frederic Tridon of University of Cologne for providing the lookup tables of SSRGA scattering properties and Samantha Nebylitsa of University of Miami for processing the MASC and Parsivel data and retrieving particle properties. We also thank Matthew Miller and Sandra Yuter of North Carolina State University for supporting the MASC observations and providing its data.

925

Financial supports.

This research was supported by the National Science Foundation grant # 1841246.



References

- 930 Andrić, J., Kumjian, M. R., Zrnić, D., Straka, J. M., and Melnikov, V.: Polarimetric signatures
above the melting layer in winter storms: An observational and modeling study. *J. Appl.
Meteorol. Climatol.*, **52**, 682–700, doi: 10.1175/JAMC-D-12-028.1, 2013
- Battaglia, A., Kollias, P., Dhillon, R., Roy, R., Tanelli, S., Lebsock, M., Grecu, M., Lamer, K.,
Watters, D., and Mroz, K., Heymsfield, G., Li, L., Furukawa, K.: Space-borne cloud and
precipitation radars: status, challenges and ways forward, *Reviews of Geophysics*, **58**,
935 e2019RG000686. <https://doi.org/10.1029/2019RG000686>, 2020.
- Battaglia, A., Mroz, K., T., Tridon, F., Tanelli, S., Tian, L., and Heymsfield, G. M.: Using a
multiwavelength suite of microwave instruments to investigate the microphysical structure of
deep convective cores, *J. Geophys. Res. Atmos.*, **121**, 9356–9381, doi:10.1002/2016JD025269,
2016
- 940 Battaglia, A., Rustemeier, E., Tokay, A., Blahak, U., and Simmer, C.: PARSIVEL Snow
Observations: A Critical Assessment, *J. Atmos. Ocean. Tech.*, **27**, 333–344,
<https://doi.org/10.1175/2009JTECHA1332.1>, 2010
- Bechini, R., Baldini, L., and Chandrasekar, V.: Polarimetric radar observations in the ice region of
precipitating clouds at C-band and X-band radar frequencies, *Appl. Meteorol. Climatol.*, **52**,
945 1147–1169, doi:10.1175/JAMC-D-12-055.1, 2013
- Böhm, H.: A general equation for the terminal fall speed of solid hydrometeors. *J. Atmos. Sci.*, **46**,
2419–2427, doi:10.1175/1520-0469(1989)046<2419:AGEFTT.2.0.CO;2, 1989.
- Colle, B.A., Stark, D., and Yuter, S.E.: Surface microphysical observations within East coast
winter storms on Long Island. *Mon. Wea. Rev.*, **142**, 3126–3146, 2014.
- 950 Dias Neto, J., Kneifel, S., Ori, D., Trömel, S., Handwerker, J., Bohn, B., Hermes, N., Mühlbauer,
K., Lenefer, M., and Simmer, C.: The TRIPLE-frequency and Polarimetric radar Experiment for
improving process observations of winter precipitation, *Earth Syst. Sci. Data*, **11**, 845–863,
<https://doi.org/10.5194/essd-11-845-2019>, 2019.
- Garrett, T. J., Fallgatter, C., Shkurko, K., and Howlett, D.: Fall speed measurement and high-
955 resolution multi-angle photography of hydrometeors in free fall. *Atmos. Meas. Tech.*, **5**, 2625–
2633, doi: <https://doi.org/10.5194/amt-5-2625-2012>, 2012.
- Garrett, T. J., and Yuter, S. E.: Observed influence of riming, temperature, and turbulence on the
fallspeed of solid precipitation, *Geophys. Res. Lett.*, **41**, 6515–6522,
doi:10.1002/2014GL061016, 2014.
- 960 Giangrande, S., Toto, T., Bansemmer, A., Kumjian, M., Mishra, S., and Ryzhkov, A.: Insights into
riming and aggregation processes as revealed by aircraft, radar, and disdrometer observations
for a 27 April 2011 widespread precipitation event. *J. Geophys. Res. Atmos.*, **121**, 5846–5863,
<https://doi.org/10.1002/2015JD024537>, 2016.
- Griffin, E. M., Schuur, T. J., and Ryzhkov, A. V.: A Polarimetric Analysis of Ice Microphysical
965 Processes in Snow, Using Quasi-Vertical Profiles, *J. Appl. Meteor. Clim.*, **57**, 31–50.
<https://doi.org/10.1175/JAMC-D-17-0033.1>, 2018
- Griffin, E., Schuur, T., and Ryzhkov, A.: A polarimetric radar analysis of ice microphysical
properties in melting layers of winter storms using S-band quasi-vertical profiles. *J. Appl.
Meteor. Clim.*, **59**, 751–767, <https://doi.org/10.1175/JAMC-D-19-0128.1>, 2020.
- 970 Heymsfield, A. J., and Westbrook, C. D.: Advances in the estimation of ice particle fall speeds
using laboratory and field measurements. *J. Atmos. Sci.*, **67**, 2469–2482,
doi:10.1175/2010JAS3379.1, 2010.



- Hogan, R. J., Gaussiat, N., and Illingworth, A. J.: Stratocumulus liquid water content from dual-wavelength radar, *J. Atmos. Ocean. Tech.*, 22(8), 1207–1218, 2005.
- 975 Hogan, R.J., Honeyager, R., Tyynelä, J. and Kneifel, S.: Calculating the millimetre-wave scattering phase function of snowflakes using the self-similar Rayleigh–Gans approximation. *Quarterly Journal of the Royal Meteorological Society*, 143, 834–844, 2017.
- Hogan, R. J., and Westbrook, C. D.: Equation for the microwave backscatter cross section of aggregate snowflakes using the self-similar Rayleigh–Gans approximation, *J. Atmos. Sci.*, 980 **71(9)**, 3292–3301, 2014.
- Huang, D., Johnson, K., Liu, Y., and Wiscombe, W.: High resolution retrieval of liquid water vertical distributions using collocated Ka-band and W-band cloud radars, *Geophys. Res. Lett.*, 36, doi:10.1029/2009gl041364, 2009.
- Hubbert, J. C., and Bringi, V. N.: An iterative filtering technique for the analysis of copolar differential phase and dual-Frequency Radar Measurements. *J. Atmos. Ocean. Tech.*, 12, 643–648, doi: 10.1175/1520-0426(1995)012<0643:AIFTFT>2.0.CO;2, 1995.
- 985 Illingworth, A. J., Barker, H., B,eljaars, A., Ceccaldi, M., Chepfer, H., Clerbaux, N., Cole, J., Delanoë, J. Domenech, C., and Donovan, D. P.: The EarthCARE satellite: The next step forward in global measurements of clouds, aerosols, precipitation, and radiation, *Bull. Amer. Meteor. Soc.*, 96(8), 1311–1332, 2015.
- 990 Jiang, Z., Oue, M., Verlinde, J., Clothiaux, E., Aydin, K., Botta, G., and Lu, Y.: What can we conclude about the real aspect ratios of ice particle aggregates from two-dimensional images? *J. Appl. Meteor. Clim.*, **56**, 725–734, 2017.
- Kajikawa, M.: Observation of the falling motion of early snowflakes. Part II: On the variation of falling velocity. *J. Meteor. Soc. Jpn.*, 67(5), 731–738, 1989.
- 995 Kalesse, H., Kollias, P., and Szyrmer, W.: On using the relationship between Doppler velocity and radar reflectivity to identify microphysical processes in midlatitudinal ice clouds. *J. Geophys. Res. Atmos.*, 118, 12168–12179, doi: 10.1002/2013JD020386, 2013.
- Kennedy, P. C., and Rutledge, S. A.: S-band dual-polarization radar observations of winter storms. *J. Appl. Meteor. Clim.*, 50, 844–858, doi:10.1175/2010JAMC2558.1, 2011.
- 1000 Kneifel, S., Lerber, A., Tiira, J., Moisseev, D., Kollias, P., and Leinonen, J.: Observed relations between snowfall microphysics and triple-frequency radar measurements. *J. Geophys. Res. Atmos.*, 120, 6034–6055, doi:10.1002/2015JD023156, 2015.
- 1005 Kneifel, S., Kollias, P., Battaglia, Al., Leinonen, J., Maahn, M., Kalesse, H., and Tridon, F.: First observations of triple-frequency radar Doppler spectra in snowfall: Interpretation and applications. *Geophys. Res. Lett.*, 43, 2225–2233, doi:10.1002/2015GL067618, 2016.
- Kneifel, S., and Moisseev, D.: Long-term statistics of riming in nonconvective clouds derived from ground-based Doppler cloud radar observations. *J. Atmos. Sci.*, 77, 10, 3495–3508, <https://doi.org/10.1175/JAS-D-20-0007.1>, 2020.
- 1010 Kollias, P., Bharadwaj, N., Clothiaux, E.E., Lamer, K., Oue, M., Hardin, J., Isom, B., Lindenmaier, I., Matthews, A., Luke, E.P., Giangrande, S.E., Johnson, K., Collis, S., Comstock, J., and Mather, J.H.: The ARM Radar Network: At the leading edge of cloud and precipitation observations. *Bull. Amer. Meteor. Soc.*, 101, E588–E607, <https://doi.org/10.1175/BAMS-D-18-0288.1,2020a>.
- 1015 Kollias, P., Bharadwaj, N., Widener, K., I. Jo, and Johnson, K.: Scanning ARM cloud radars. Part I: Operational sampling strategies. *J. Atmos. Ocean. Tech.*, 31, 569–582, doi:10.1175/JTECH-D-13-00044.1, 2014.



- 1020 Kollias, P., Clothiaux, E. E., Ackerman, T. P., Albrecht, B. A., Widener, K. B., Moran, K. P.,
Luke, E. P., Johnson, K. L., Bharadwaj, N., Mead, J. B., Miller, M. A., Verlinde, J.,
Marchand, R. T., and Mace, G. G.: Development and Applications of ARM Millimeter-
Wavelength Cloud Radars. *Meteorological Monographs* 57, 17.1-17.19,
<https://doi.org/10.1175/AMSMONOGRAPHS-D-15-0037.1>, 2016.
- 1025 Kollias, P., Clothiaux, E. E., Miller, M. A., Albrecht, B. A., Stephens, G. L., and Ackerman, T.
P.: Millimeter-Wavelength Radars: New Frontier in Atmospheric Cloud and Precipitation
Research, *Bulletin of the American Meteorological Society*, 88(10), 1608-1624, 2007.
- Kollias, P., Luke, E., Oue, M., and Lamer, K.: Agile adaptive radar sampling of fast evolving
atmospheric phenomena guided by satellite imagery and surface cameras, *Geophys. Res. Lett.*,
47(14), e2020GL088440, 2020b.
- 1030 Korolev, A. V., and Isaac, G.: Roundness and aspect ratio of particles in ice clouds. *J. Atmos. Sci.*,
60, 1795–1808, doi:10.1175/1520-0469(2003)060<1795:RAAROP>2.0.CO;2, 2003.
- Kumjian, M. R., and Lombardo, K. A.: Insights into the evolving microphysical and kinematic
structure of Northeastern U.S. winter storms from dual-polarization Doppler radar. *Mon. Wea.*
Rev., 145, 1033-1061, doi: 10.1175/MWR-D-15-0451.1, 2017.
- 1035 Kumjian, M. R., Mishra, S., Giangrande, S. E., Toto, T., Ryzhkov, A. V., and Bansemer, A.:
Polarimetric radar and aircraft observations of saggy bright bands during MC3E. *Journal of*
Geophysical Research, **121**, 3584–3607, doi:10.1002/2015JD024446, 2016.
- Kumjian, M. R., Rutledge, S. A., Rasmussen, R. M., Kennedy, P. C., and Dixon, M.: High-
resolution polarimetric radar observations of snow generating cells. *Journal of Applied*
Meteorology and Climatology, **53**, 1636–1658, doi: 10.1175/JAMC-D-13-0312.1, 2014.
- 1040 Kumjian, M. R., Tobin, D. M., Oue, M., and Kollias, P.: Microphysical Insights into Ice Pellet
Formation Revealed by Fully Polarimetric Ka-band Doppler Radar. *J. Appl. Meteor. Climatol.*,
doi: <https://doi.org/10.1175/JAMC-D-20-0054.1>, 2020
- 1045 Lamer, K., Oue, M., Battaglia, A., Roy, R. J., Cooper, K. B., Dhillon, R., and Kollias, P.: First
Light Multi-Frequency Observations with a G-band radar, *Atmos. Meas. Tech. Discuss.*
[preprint], <https://doi.org/10.5194/amt-2020-493>, in review, 2020.
- Leinonen, J., and Moisseev, D.: What do triple-frequency radar signatures reveal about aggregate
snowflakes?, *J. Geophys. Res. Atmos.*, 120, 229–239, doi:10.1002/2014JD022072, 2015.
- Leinonen, J., Moisseev, D., and Nousiainen, T.: Linking snowflake microstructure to multi-
frequency radar observations, *J. Geophys. Res. Atmos.*, 118, 3259–3270, doi:
1050 <http://dx.doi.org/10.1002/jgrd.50163>, 2013.
- Leinonen, J. and Szyrmer, W.: Radar signatures of snowflake riming: a modeling study. *Earth and*
Space Science 2: 346–358, doi:10.1002/2015EA000102, 2015.
- Lewis, E. R., and Coauthors, 2012: MAGIC: Marine ARM GPCI Investigation of Clouds.
DOE/SC-ARM-12-020, U.S. Department of Energy, 12 pp.
- 1055 Li, H., Moisseev, D., and von Lerber, A.: How does riming affect dual-polarization observations
and snowflake shape? *J. Geophys. Res.*, **123** (11), 6070 – 6081, 2018.
- Liebe, H. J., Hufford, G., and Cotton, M.: Propagation modeling of moist air and suspended
water/ice particles at frequencies below 1000 GHz, presented at an AGARD Meeting on
'Atmospheric Propagation Effects through Natural and Man-Made Obscurants for Visible to
1060 MM-Wave Radiation,' May, 1993.
- Locatelli, J. D., and Hobbs, P. V.: Fall speeds and masses of solid precipitation particles, *Geophys.*
Res. Atmos., 79(15), 2185-2197, 1974.



- 1065 Löffler-Mang, M., and Blahak, U.: Estimation of the Equivalent Radar Reflectivity Factor from Measured Snow Size Spectra. *J. Appl. Meteor.*, **40**, 843–849, doi: [https://doi.org/10.1175/1520-0450\(2001\)040<0843:EOTERR>2.0.CO;2](https://doi.org/10.1175/1520-0450(2001)040<0843:EOTERR>2.0.CO;2), 2001.
- 1070 Luke, E., Kollias, P., and Shupe, M. D.: Detection of supercooled liquid in mixed-phase clouds using radar Doppler spectra. *J. Geophys. Res. Atmos.*, **115**, D19201, doi:10.1029/2009JD012884, 2010.
- 1075 Mason, S. L., Hogan, R. J., Westbrook, C. D., Kneifel, S., Moisseev, D., and von Terzi, L.: The importance of particle size distribution and internal structure for triple-frequency radar retrievals of the morphology of snow, *Atmos. Meas. Tech.*, **12**, 4993–5018, <https://doi.org/10.5194/amt-12-4993-2019>, 2019.
- 1075 Mather, J. H., and Voyles, J. W.: The Arm Climate Research Facility: A review of structure and capabilities. *Bull. Amer. Meteor. Soc.*, **94**, 377–392, doi: 10.1175/BAMS-D-11-00218.1, 2013.
- 1075 Matrosov, S. Y.: Theoretical study of radar polarization parameters obtained from cirrus clouds. *J. Atmos. Sci.*, **48**, 1062–1070, [https://doi.org/10.1175/1520-0469\(1991\)048<1062:TSORPP>2.0.CO;2](https://doi.org/10.1175/1520-0469(1991)048<1062:TSORPP>2.0.CO;2), 1991
- 1080 Matrosov, S. Y.: A dual-wavelength radar method to measure snowfall rate. *J. Appl. Meteor.*, **37**, 11, 1510–1521, [https://doi.org/10.1175/1520-0450\(1998\)037<1510:ADWRMT>2.0.CO;2](https://doi.org/10.1175/1520-0450(1998)037<1510:ADWRMT>2.0.CO;2), 1998
- 1085 Matrosov, S.Y.: Polarimetric radar variables in snowfall at Ka- and W-band frequency bands: A comparative analysis. *J. Atmos. Oceanic Technol.*, **38**, 91–101, <https://doi.org/10.1175/JTECH-D-20-0138.1>, 2021.
- 1085 Matrosov, S.Y., Mace, G.G., Marchand, R., Shupe, M.D., Hallar, A.G. and McCubbin, I.B.: Observations of ice crystal habits with a scanning polarimetric W-band radar at slant linear depolarization ratio mode. *J. Atmos. Oceanic Technol.*, **29**, 989–1008. <https://doi.org/10.1175/JTECH-D-11-00131.1>, 2012
- 1090 Matrosov, S. Y., Schmitt, C. G., Maahn, M., and de Boer, G.: Atmospheric ice particle shape estimates from polarimetric radar measurements and in situ observations. *J. Atmos. Oceanic Technol.*, **34**, 2569–2587, doi: 10.1175/JTECH-D-17-0111.1, 2017.
- 1095 Matrosov, S.Y., Maahn, M., and de Boer, G.: Observational and modeling study of ice hydrometeor radar dual-wavelength ratios. *J. Appl. Meteor. Climatol.*, **58**, 2005–2017. <https://doi.org/10.1175/JAMC-D-19-0018.1>, 2019
- 1095 Matrosov, S.Y., Ryzhkov, A.V., Maahn, M., and de Boer, G.: Hydrometeor shape variability in snowfall as retrieved from polarimetric radar measurements. *J. Appl. Meteor. Climatol.*, **59**, 1503–1517. <https://doi.org/10.1175/JAMC-D-20-0052.1>, 2020
- 1100 Mitchell, D. L.: Use of mass- and area-dimensional power laws for determining precipitation particle terminal velocities. *J. Atmos. Sci.*, **53**, 1710–1723, doi:10.1175/1520-0469(1996)053<1710:UOMAAD>2.0.CO;2, 1996.
- 1100 Mitchell, D. L., and Heymsfield, A. J.: Refinements in the treatment of ice particle terminal velocities, highlighting aggregates. *J. Atmos. Sci.*, **62**, 1637–1644, doi:10.1175/JAS3413.1, 2005.
- 1105 Moisseev, D. N., Lautaportti, S., Tyynela, J., and Lim, S.: Dual-polarization radar signatures in snowstorms: Role of snowflake aggregation. *J. Geophys. Res. Atmos.*, **120**, 12644–12655, doi:10.1002/2015JD023884, 2015.
- 1105 Moisseev, D., von Lerber, A., and Tiira, J.: Quantifying the effect of riming on snowfall using ground-based observations, *J. Geophys. Res.-Atmos.*, **122**, 4019–4037, 2017



- 1110 Myagkov, A., Seifert, P., Wandinger, U., Bühi, J., and Engelmann, R.: Relationship between temperature and apparent shape of pristine ice crystals derived from polarimetric cloud radar observations during the ACCEPT campaign. *Atmos. Meas. Tech.*, **9**, 3739-3754, doi: 0.5194/amt-9-3739-2016, 2016.
- Orr, B. W., and Kropfli, R.: A method for estimating particle fall velocities from vertically pointing Doppler radar. *J. Atmos. Oceanic Technol.*, **16**, 29–37, doi: 10.1175/1520-0426(1999)016<0029:AMFEPF>2.0.CO;2, 1999.
- 1115 Oue, M., Kumjian, M. R., Y. Lu, Verlinde, J., Aydin, K., and Clothiaux, E. E.: Linear depolarization ratios of columnar ice crystals in a deep precipitating system over the Arctic observed by zenith-pointing Ka-band Doppler radar. *J. Appl. Meteor. Clim.*, **54**, 1060-1068, doi: 10.1175/JAMC-D-15-0012.1, 2015.
- Oue, M., Galletti, M., Verlinde, J., Ryzhkov, A., and Lu, Y.: Use of X-Band differential reflectivity measurements to study shallow Arctic mixed-phase clouds. *J. Appl. Meteor. Clim.*, **55**, 403-424, doi: 10.1175/JAMC-D-15-0168.1, 2016.
- Oue, M., Kollias, P., Ryzhkov, A., and Luke, E.: Toward exploring the synergy between cloud radar polarimetry and Doppler spectral analysis in deep cold precipitating systems in the Arctic. *J. Geophys. Res.* vol. 123, 2797 – 2815, doi: 10.1002/2017JD027717, 2018.
- 1125 Peters, G., Fischer, B., Andersson, T.: Rain observations with a vertically looking Micro Rain Radar (MRR). *Boreal Environ Res.* 7:353–362, 2002
- Protat, A., and Williams, C. R.: The accuracy of radar estimates of ice terminal fall speed from vertically pointing Doppler radar measurements. *J. Appl. Meteor. Clim.* **50**, 2120-2138, doi: 10.1175/JAMC/-D-10-05031.1, 2011
- 1130 Pruppacher, H. R., and Klett, J. D.: *Microphysics of clouds and precipitation*. Springer Dordrecht Heidelberg London New York, 975p, doi: 10.1007/978-0-306-48100-0, 2010.
- Reinking, R.F., Matrosov, S.Y. Kropfli, R.A. and Bartram, B.W.: Evaluation of a 45-degree slant quasi-linear radar polarization state for distinguishing drizzle droplets, pristine ice crystals, and less regular ice particles. *J. Atmos. Oceanic Technol.*, **19**, 296-321. <https://doi.org/10.1175/1520-0426-19.3.296>, 2002
- 1135 Rosenkranz, P. W.: Water vapor microwave continuum absorption: A comparison of measurements and models, *Radio Sci.*, 33(4), 919– 928, doi:10.1029/98RS01182, 1998.
- Ryzhkov, A. V., Zhang, P., Reeves, H. D., Kumjian, M. R., Tschallener, T., Trömel, S., and Simmer, C.: Quasi-vertical profiles – A new way to look at polarimetric radar data. *J. Atmos. Ocean. Tech.*, **33**, 551-562, doi: 10.1175/JTECH-D-15-0020.1, 2016
- 1140 Ryzhkov, A. V., Zrnić, D. S., and Gordon, B. A.: Polarimetric method for ice water content determination. *J. Appl. Meteor.*, **37**, 125–134, doi: 10.1175/1520-0450(1998)037<0125:PMFIWC>2.0.CO;2, 1998.
- Schneebeli, M., Dawes, N., Lehning, M., & Berne, A. (2013). High-resolution vertical profiles of X-band polarimetric radar observables during snowfall in the Swiss Alps. *Journal of Applied Meteorology and Climatology*, **52**, 378-394, doi: 10.1175/JAMC-D-12-015.1.
- Schrom, R. S., and Kumjian, M. R.: Connecting microphysical processes in Colorado Winter storms with vertical profiles of radar observations. *J. Appl. Meteor. Clim.*, **55**, 1771–1787, doi: 10.1175/JAMC-D-15-0338.1, 2016.
- 1150 Schrom, R. S., Kumjian, M. R., and Lu, Y.: Polarimetric radar signatures of dendritic growth zones within Colorado winter storms. *J. Appl. Meteor. Clim.*, **54**, 2365-2388, doi: 10.1175/JAMC-D-15-0004.1, 2015.



- 1155 Sinclair, V. A., Moisseev, D., and von Lerber, A.: How dual-polarization radar observations can be used to verify model representation of secondary ice. *J. Geophys. Res. Atmos.*, 121, 10,954–10,970, doi:10.1002/2016JD025381, 2016.
- Stokes, G. M., and Schwartz, S. E.: The Atmospheric Radiation Measurement (ARM) Program: Programmatic Background and Design of the Cloud and Radiation Test Bull. *Amer. Meteor. Soc.*, 75, 7, 1201-1222, [https://doi.org/10.1175/1520-0477\(1994\)075<1201:TARMPP>2.0.CO;2](https://doi.org/10.1175/1520-0477(1994)075<1201:TARMPP>2.0.CO;2), 1994.
- 1160 Szyrmer, W., and Zawadzki, I.: Snow Studies. Part II: Average relationship between mass of snowflakes and their terminal fall velocity. *J. Atmos. Sci.* 67, 10, 3319-3335, <https://doi.org/10.1175/2010JAS3390.1>, 2010.
- 1165 Tridon, F., Battaglia, A., Chase, R. J., Turk, F. J., Leinonen, J., Kneifel, S., Mroz, K., Finlon, J., Bansemmer, A., and Tanelli, S.: The microphysics of stratiform precipitation during OLYMPEX: Compatibility between triple-frequency radar and airborne in situ observations, *J. Geophys. Res. Atmos.*, 124(15), 8764-8792, 2019.
- Tridon, F., Battaglia, A., and Kneifel, S.: Estimating total attenuation using Rayleigh targets at cloud top: applications in multilayer and mixed-phase clouds observed by ground-based multifrequency radars, *Atmos. Meas. Tech.*, 13(9), 5065-5085, 2020.
- 1170 Tridon, F., Battaglia, A., and Kollias, P.: Disentangling Mie and attenuation effects in rain using a Ka/W dual-wavelength Doppler spectral ratio technique. *Geophys. Res. Lett.*, 40 (20), 5548–5552, doi:10.1002/2013GL057454, 2013.
- 1175 Troemel, S., Ryzhkov, A., Hickman, B., Muhlbauer, K., and Simmer, C.: Polarimetric radar variables in the layers of melting and dendritic growth at X band – implications for a nowcasting strategy in stratiform rain. *J. Appl. Meteor. Clim.*, 58, 2497 – 2522, 2019
- Tyynelä, J., Leinonen, J., Moisseev, D., and Nousiainen, T.: Radar backscattering from snowflakes: Comparison of fractal, aggregate and soft-spheroid models, *J. Atmos. Oceanic Technol.*, 28, 1365–1372, doi:10.1175/JTECH-D-11-00004, 2011.
- 1180 Vivekanandan, J., Bringi, V., Hagen, M., and Meischner, P.: Polarimetric radar studies of atmospheric ice particles. *IEEE Trans. on Geosci. Remote Sens.*, 32, 1 –10, 1994.
- von Lerber, A., Moisseev, D., Bliven, L. F., Petersen, W., Harri, A.-M., and Chandrasekar, V.: Microphysical Properties of Snow and Their Link to Ze–S Relations during BAECC 2014. *J. Appl. Meteor. Climatol.*, 56, 1561–1582, <https://doi.org/10.1175/JAMC-D-16-0379.1>, 2017.
- 1185 Williams, E., Smalley, D., Donovan, M., Hallowell, R., Hood, K., Bennett, B., Evaristo, R., Stepanek, A., Bals-Elsholz, T., Cobb, J., Ritzman, J., Korolev, A., and Wolde, M.: Measurements of differential reflectivity in snowstorms and warm season stratiform systems. *J. Appl. Meteor. Clim.*, 54, 573–595, doi: 10.1175/JAMC-D-14-0020.1, 2015.
- 1190 Zawadzki, I., Fabry, F., and Szyrmer, W.: Observations of supercooled water and secondary ice generation by a vertically pointing X-band Doppler radar. *Atmos. Res.*, 59–60, 343–359, doi: 10.1016/S0169-8095(01)00124-7, 2001.
- Zhu, Z., Lamer, K., Kollias, P., and Clothiaux, E. E.: The vertical structure of liquid water content in shallow clouds as retrieved from dual-wavelength radar observations, *J. Geophys. Res. Atmos.*, 124(24), 14184-14197, 2019